

# Chapter 2

## NMR in Inhomogeneous Fields

Federico Casanova and Juan Perlo

### 2.1 Introduction

Besides the redesigning of the hardware to excite and detect NMR signals from sample volumes external to the sensor, the field of single-sided NMR has required special effort for adapting or developing new measurement techniques suitable to work in the presence of inhomogeneous  $B_0$  and  $B_1$  fields [1–4]. When large samples are studied in the presence of an inhomogeneous  $B_0$  field, the spectral bandwidth of the spin system easily exceeds the rf field strength  $B_1$  and all rf pulses act as selective pulses. The spatial dependence of both the resonance frequency and the amplitude of the radiofrequency field makes it impossible to impart a uniform rotation to all excited spins, leading to a distribution of flip angles across the sample. Although the pulse can be set to define a  $90^\circ$  rotation in a certain part of the object chosen to be on-resonance, the magnetization in near voxels will experience an  $\alpha$  rotation quickly departing from the desired angle. Consequently, instead of converting longitudinal magnetization into transverse magnetization (assuming the pulse is applied to the sample in thermal equilibrium) a pulse  $\alpha$  takes part of the magnetization to the transverse plane, but leaves considerable magnetization along the longitudinal axis. These two types of magnetization evolve in completely different ways during a subsequent free evolution period and they are referred to as different coherence pathways. As we will see, pulse imperfections give rise to a number of coherence pathways that dramatically increase with the number of pulses. Each of these pathways exhibits a characteristic attenuation by relaxation and molecular self-diffusion and depends on the phase of the rf pulses according to the transitions caused by the pulses. While longitudinal magnetization relaxes with  $T_1$  and is not affected by the presence of a field gradient, transverse magnetization relaxes with  $T_2$  and is spread out by a  $B_0$  gradient. Moreover, whereas the transverse magnetization generated by a single pulse has a phase proportional to the phase of the pulse, the remaining longitudinal magnetization has no memory of such phase. The unwanted interference

---

F. Casanova and J. Perlo (✉)

Institut für Technische Chemie und Makromolekulare Chemie, RWTH Aachen University,  
D-52074 Aachen, Germany

of the different pathways during signal detection has required re-examination of the spin system response to most pulse sequences known from NMR in homogeneous fields in order to find cycles for the phases of the rf pulses that lead to elimination of non-desired pathways.

This chapter provides the tools necessary to calculate the evolution of a non-interacting  $\frac{1}{2}$  spin system in inhomogeneous  $B_0$  and  $B_1$  fields. To describe the dynamics of the magnetization in a vectorial picture, the effect of rf pulses and free evolution periods is first described in the  $\{M_x, M_y, M_z\}$  basis set. Then, a basis set is described which is more convenient to separate the magnetization into the different coherence pathways created by an inhomogeneous and off-resonance rf field. This second formalism is more convenient to identify and filter non-desired signals. Both formalisms provide the dynamics of the spin system for a given  $B_0$  and  $B_1$  spatial distribution. In the next sections these numerical tools are used to calculate the response of a spin system to well-known sequences such as the Hahn echo [5]; CPMG (Carr-Purcell-Meiboom-Gill) [6, 7]; inversion and saturation recovery; and stimulated echo, which are the key sequences to measure longitudinal and transverse relaxation times; and molecular self-diffusion. The analysis is made first by including the off-resonance condition defined in an inhomogeneous  $B_0$  field, but assuming a homogeneous  $B_1$  field. Then, the complications introduced by the excitation with an inhomogeneous radiofrequency field are evaluated by including in the simulations the field generated by a surface rf coil. Finally, how to calculate the signal-to-noise ratio in a strongly inhomogeneous field is discussed. Based on the provided equations both magnet and rf coil geometry can be optimized in order to maximize the sensitivity of the sensor.

### 2.1.1 Evolution of the Magnetization During a Pulse Sequence

Every pulse sequence can be considered as a succession of two types of events, i.e., rf pulses and free evolution periods. The effect of each of these events on the magnetization can be described by a rotation represented by a  $3 \times 3$  matrix. Thus, the evolution of the components of the magnetization vector  $\mathbf{M}(t) = (M_x, M_y, M_z)$  under a pulse sequence composed of  $n$  events involves simply the product of  $n$  matrixes:

$$\mathbf{M}(t) = \prod_{i=1}^n R_{\hat{\eta}_i}(\epsilon_i) \mathbf{M}(0),$$

where  $\mathbf{M}(0) = (0, 0, M_0)$  and  $\mathbf{M}(t)$  are the equilibrium magnetization and the magnetization at a time  $t$  after the application of the sequence, respectively [8]. The  $R_{\hat{\eta}_i}$  matrices represent rotations by an angle  $\epsilon_i$  about an axis  $\hat{\eta}_i$ . In the case of applying an rf field with amplitude  $B_1$ , frequency  $\omega_{\text{rf}}$ , and phase  $\phi$ , the magnetization precesses about an effective field of amplitude

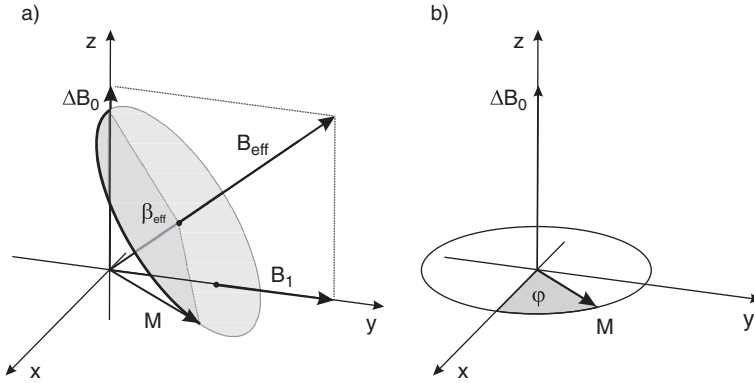


**Fig. 2.1** (a) Precession of the magnetization vector about the tilted effective magnetic field  $B_{\text{eff}}$  during the application of an rf field with amplitude  $B_1$ , phase  $\pi/2$ , and offset resonance  $\Delta\omega_0 = \gamma \Delta B_0$ . (b) Precession about the off-set field  $\Delta B_0$  during a free evolution period, which is simply a rotation about the  $z$ -axis

$$B_{\text{eff}} = \sqrt{B_1^2 + \Delta B_0^2}, \quad (2.1)$$

which is tilted with respect to the  $z$ -axis by an angle

$$\theta = \tan^{-1}(B_1/\Delta B_0), \quad (2.2)$$

where  $\Delta B_0 = B_0 - \omega_{\text{rf}}/\gamma$ . Figure 2.1a shows the cone described by the magnetization precessing about the effective field for an rf pulse applied with phase  $\phi = \pi/2$ . The effective angle nutated about  $B_{\text{eff}}$  during a pulse of duration  $t_p$  is given by:

$$\beta_{\text{eff}} = \gamma B_{\text{eff}} t_p. \quad (2.3)$$

The components of the magnetization after the rf pulse can be calculated by rotating the vector about the effective field by an angle  $\beta_{\text{eff}}$ . To perform this rotation it is convenient to transform the magnetization before the pulse to a local frame with the  $z$ -axis along  $B_{\text{eff}}$  and the  $x$ -axis lying in the plane defined by the vectors  $B_{\text{eff}}$  and  $B_1$ . Depending on the phase  $\phi$  of the rf pulse the general rotation is given by

$$\mathbf{A} = \begin{pmatrix} \cos \theta \cos \phi & \cos \theta \sin \phi & -\sin \theta \\ -\sin \phi & \cos \phi & 0 \\ \sin \theta \cos \phi & \sin \theta \sin \phi & \cos \theta \end{pmatrix}.$$

Once the magnetization vector is in the new basis, it is rotated by an angle  $\beta_{\text{eff}}$  about the effective field by applying the matrix

$$\mathbf{B} = \begin{pmatrix} \cos \beta_{\text{eff}} & -\sin \beta_{\text{eff}} & 0 \\ \sin \beta_{\text{eff}} & \cos \beta_{\text{eff}} & 0 \\ 0 & 0 & 1 \end{pmatrix}.$$

Then, the vector is transformed back to the original coordinate system by applying the inverse rotation

$$\mathbf{A}^{-1} = \begin{pmatrix} \cos \theta \cos \phi & -\sin \phi & \sin \theta \cos \phi \\ \cos \theta \sin \phi & \cos \phi & \sin \theta \sin \phi \\ -\sin \theta & 0 & \cos \theta \end{pmatrix}. \quad (2.4)$$

The total effect of the rf pulse is simply calculated as the product of the three matrices

$$\mathbf{P} = \mathbf{A}^{-1} \mathbf{B} \mathbf{A}. \quad (2.5)$$

During free evolution periods, the magnetization simply precesses about the offset field  $\Delta B_0$  with a frequency  $\Delta \omega_0$  (see Fig. 2.1b), and the components of the magnetization after a time  $\tau$  can be calculated as  $\mathbf{M}(t + \tau) = \mathbf{E} \mathbf{M}(t)$ , where

$$\mathbf{E} = \begin{pmatrix} e_2(\tau) \cos \Delta \omega_0 \tau & e_2(\tau) \sin \Delta \omega_0 \tau & 0 \\ e_2(\tau) \sin \Delta \omega_0 \tau & e_2(\tau) \cos \Delta \omega_0 \tau & 0 \\ 0 & 0 & e_1(\tau) \end{pmatrix}. \quad (2.6)$$

The effects of longitudinal and transverse relaxation are included during free evolution periods via the attenuation factors  $e_1(\tau) = \exp(-\tau/T_1)$  and  $e_2(\tau) = \exp(-\tau/T_2)$ , but they are usually neglected during rf pulses. The factor  $e_1$  includes  $T_1$  attenuation but does not take into account the magnetization created during each free evolution period. To include the new magnetization after a free evolution  $\tau$ , a vector  $\mathbf{M}_{\text{new}}(\tau) = (0, 0, 1 - \exp(-\tau/T_1))$  must be added to the resultant magnetization at the end of the evolution period. In this way, after a free evolution  $\tau$ , the magnetization is given by  $\mathbf{M}(t + \tau) = \mathbf{E} \mathbf{M}(t) + \mathbf{M}_{\text{new}}(\tau)$ . Using this formalism, the evolution of the magnetization under defined  $B_0$  and  $B_1$  fields can be calculated at any time of the sequence by applying the right number of rotations to the initial magnetization vector. The strategy to integrate the total signal response of a spin system to a particular sequence requires partitioning of the sample into small voxels where a uniform resonance frequency and rf amplitude can be defined. In Sect. 2.2 this approach to calculate the dynamics of the magnetization will be used to analyze the response to different pulse sequences.

### 2.1.2 Separation of the Magnetization into Coherence Pathways

The formalism presented in Sect. 2.1.1 describes the evolution of the magnetization in the vector basis set  $\{M_x, M_y, M_z\}$ . This basis set is convenient from a graphical

point of view, because it provides the trajectory of the magnetization vector during the pulse sequence. However, when a number of pulses is applied with arbitrary phases, separation of the magnetization into different pathways with defined evolution becomes extremely complicated, if not impossible. In this basis set, longitudinal and transverse magnetization can be separated, but dephasing and rephasing transverse magnetization cannot be identified in a simple way. An example where these two types of coherence are generated is in a spin echo sequence. In this case, magnetization dephasing during the time between the first and second rf pulses is converted into refocusing magnetization that leads to the echo formation at a defined time after the second pulse. However, if the second pulse does not define a perfect  $180^\circ$  rotation, part of the dephasing magnetization keeps dephasing after the second pulse. This coherence is known to be responsible for one of the four echoes generated after the application of a third rf pulse. A basis set where the magnetization is split into the three mentioned coherence states is the one defined as

$$\begin{aligned} M_{+1} &= M_x + iM_y, \\ M_{-1} &= M_x - iM_y, \\ M_0 &= M_z, \end{aligned} \quad (2.7)$$

where  $M_{+1}$  is the dephasing,  $M_{-1}$  the rephasing, and  $M_0$  the longitudinal magnetization, which are designated as  $q = +1, -1$ , and  $0$ , respectively [9].

Following the notation used by Hürlimann [4], the evolution under a free precession period of duration  $\tau$  is described by the matrix

$$\mathbf{\Gamma} = \begin{pmatrix} e_2 e^{(i\Delta\omega_0\tau)} & 0 & 0 \\ 0 & e_2 e^{(-i\Delta\omega_0\tau)} & 0 \\ 0 & 0 & e_1 \end{pmatrix}, \quad (2.8)$$

where, as defined in Sect. 2.1.1,  $e_1(\tau) = \exp(-\tau/T_1)$  and  $e_2(\tau) = \exp(-\tau/T_2)$  are the factors that describe attenuation by relaxation during a free evolution period. As this matrix has only diagonal elements, coherence pathways are not mixed during free precession,  $M_{+1}$  and  $M_{-1}$  are just multiplied by a phase term that depends on the offset frequency. Radiofrequency pulses, on the contrary, mix all the states according to the rotation

$$\mathbf{\Lambda} = \begin{pmatrix} \Lambda_{+1,+1} & \Lambda_{+1,-1} & \Lambda_{+1,0} \\ \Lambda_{-1,+1} & \Lambda_{-1,-1} & \Lambda_{-1,0} \\ \Lambda_{0,+1} & \Lambda_{0,-1} & \Lambda_{0,0} \end{pmatrix}. \quad (2.9)$$

The complex matrix elements of  $\mathbf{\Lambda}$  for a pulse of duration  $t_p$ , offset frequency  $\Delta\omega_0$ , amplitude  $B_1$ , effective nutation frequency  $\Omega = \gamma B_{\text{eff}}$ , and phase  $\phi$  are [4, 10]

$$\begin{aligned}
\Lambda_{+1,+1} &= \frac{1}{2} \left\{ \left( \frac{\omega_1}{\Omega} \right)^2 + \left[ 1 + \left( \frac{\Delta\omega_0}{\Omega} \right)^2 \right] \cos(\Omega t_p) \right\} + i \left( \frac{\Delta\omega_0}{\Omega} \right) \sin(\Omega t_p), \\
\Lambda_{0,0} &= \left( \frac{\Delta\omega_0}{\Omega} \right)^2 + \left( \frac{\omega_1}{\Omega} \right)^2 \cos(\Omega t_p), \\
\Lambda_{+1,0} &= \frac{\omega_1}{\Omega} \left\{ \frac{\Delta\omega_0}{\Omega} [1 - \cos(\Omega t_p)] - i \sin(\Omega t_p) \right\} \exp(+i\phi), \\
\Lambda_{0,+1} &= \frac{1}{2} \frac{\omega_1}{\Omega} \left\{ \frac{\Delta\omega_0}{\Omega} [1 - \cos(\Omega t_p)] - i \sin(\Omega t_p) \right\} \exp(-i\phi), \\
\Lambda_{+1,-1} &= \frac{1}{2} \left( \frac{\omega_1}{\Omega} \right)^2 [1 - \cos(\Omega t_p)] \exp(+i2\phi), \\
\Lambda_{-1,-1} &= \Lambda_{+1,+1}^*, \\
\Lambda_{-1,0} &= \Lambda_{+1,0}^*, \\
\Lambda_{0,-1} &= \Lambda_{0,+1}^*, \\
\Lambda_{-1,+1} &= \Lambda_{+1,-1}^*. \tag{2.10}
\end{aligned}$$

As the three states are mixed only during the application of rf pulses, Kaiser et al. [9] proposed a simple indexing where a particular coherence pathway is described by an array of numbers  $q_0, q_1, q_2, \dots, q_N$ , where  $q_k$  denotes the coherence after the  $k$ th pulse. For example, a coherence pathway after applying  $N$  rf pulses separated by free evolution periods of duration  $t_k$  is calculated as

$$\begin{aligned}
M_{q_0, q_1, q_2, \dots, q_N} &= \prod_{k=1}^N \Lambda_{q_k, q_{k-1}}^k \times \exp \left( i \Delta\omega_0 \sum_{k=1}^N q_k t_k \right) \\
&\times \exp \left( - \sum_{k=1}^N \left( \frac{q_k^2}{T_2} + \frac{1 - q_k^2}{T_1} \right) t_k \right), \tag{2.11}
\end{aligned}$$

where  $q_0 = 0$  when the system is assumed to be initially in thermal equilibrium.

In this expression, we can identify the inherent beauty of this formalism. First, each particular pathway depends on the phase of the rf pulses via the coefficients of the matrix  $\Lambda^k$  that communicate the state before the  $k$ th pulse with the state after the pulse. For example, if  $q_{k-1} = -1$  and  $q_k = +1$ , the  $k$ th matrix element in the product of Eq. (2.11)  $\Lambda_{q_k, q_{k-1}}^k = \Lambda_{+1, -1}^k$ , which depends on the phase of the  $k$ th pulse as  $\exp(+i2\phi_k)$  (see Eq. 2.10). After multiplying the  $\Lambda^k$  coefficients defining the pathway, a final phase factor is obtained that depends on the phase of the rf pulses in a characteristic way. As we will see, this phase can be exploited to define a proper phase cycle that cancels unwanted terms. The second advantage of this formalism comes from the fact that the phase accumulated during free precession periods is simply added or subtracted depending on the sign of  $q_k$ , if during the  $k$ th interval the magnetization is stored as longitudinal magnetization  $q_k = 0$  and no phase is accumulated. If after the  $N$  pulses there is a time  $t_N$  when the condition

$$\sum_{k=1}^N q_k t_k = 0 \quad (2.12)$$

is fulfilled, the coherence pathway generates an echo. If the times  $t_k$  are much larger than  $T_2^*$ , the free induction decay (FID) generated by the pulse  $k$  will be completely dephased during  $t_k$  and will not contribute to the signal detected in posterior free evolution times. In general, for single-sided sensors, this condition is well fulfilled and pathways which do not satisfy Eq. (2.12) are discarded. It must be noted that magnetization brought to the plane for the first time by the pulse  $N$  does not fulfill Eq. (2.12) during the period  $t_N$ . However, it should be retained for the signal calculation during  $t_N$ , because it does generate a signal that starts dephasing after the pulse and, depending on the timing of the sequence, may interfere with the desired signal. Finally, the last factor in Eq. (2.11) is the attenuation that the magnetization suffers due to relaxation.

A last important fact to be noted when using this formalism is that the following relation between pathways is fulfilled:

$$M_{-q_0, -q_1, -q_2, \dots, -q_N} = M_{q_0, q_1, q_2, \dots, q_N}^* \quad (2.13)$$

This means that, except for the pathway where the magnetization evolves always as longitudinal magnetization ( $M_{0,0,0,\dots,0}$ ), all the others have a twin pathway containing basically the same information. Twin pathways do not need to be taken into account in the signal calculation and it is done by selecting from the paths generating echoes only those ending with  $q_N = +1$ . As a convention, it is held that only coherence  $+1$  contributes to the signal. Then, the total signal can be calculated as

$$S_{\text{Re}} + i S_{\text{Im}} = \sum_{q_1, \dots, q_{N-1}} (\text{Re}(M_{q_0, q_1, q_2, \dots, +1}) + i \text{Im}(M_{q_0, q_1, q_2, \dots, +1})). \quad (2.14)$$

To illustrate how to proceed at the time of selecting a particular pathway, a pulse sequence composed of three arbitrary rf pulses with phases  $\phi_1$ ,  $\phi_2$ , and  $\phi_3$  is analyzed in the following. To do this, the pathways generating signal during each evolution time are analyzed. The expanding tree of coherence pathways under the application of three rf pulses is shown in Fig. 2.2 [9]. The first pulse generates  $3^1$  pathways, but only  $M_{+1}$  gives a signal and corresponds to the FID generated by the first pulse (FID<sub>1</sub>). When the second pulse is applied after a time  $t_1$ , it splits the three initial pathways into  $3^2 = 9$  paths. To find out which of these paths generate a signal during  $t_2$  is not relevant if they generated a signal during  $t_1$ . The strategy is to identify out of the total number of pathways those with  $q_2 = +1$ . So, the potential candidates to generate a signal during  $t_2$  are  $M_{0,+1,+1}$ ,  $M_{0,-1,+1}$ , and  $M_{0,0,+1}$ . The first one is magnetization brought to the transverse plane by the first pulse and is not affected by the second one. If  $t_1 \gg T_2^*$ , this path does not generate any signal during  $t_2$  because at the time the second pulse is applied, the coherence is fully dephased. The second path describes magnetization that dephases during  $t_1$  and refocuses dur-

ing  $t_2$  to generate the Hahn echo. The third pathway describes the magnetization that remains along the  $z$ -axis after the first pulse but is brought to the transverse plane by the second pulse to generate the FID observed after the second pulse ( $\text{FID}_2$ ). These two last paths interfere during  $t_2$ ; to separate them, the phase of the pulses must be cycled. As it can be easily observed, by explicitly writing Eq. (2.11) for these two particular pathways, the phase of the Hahn echo depends on the phase of the rf pulses as  $-\phi_1 + 2\phi_2$ . Moreover, the phase of the  $\text{FID}_2$  only depends on the phase of the second pulse as  $\phi_2$ . A typical phase cycle used to cancel the  $\text{FID}_2$  combines two experiments where the phase of the first pulse is incremented from 0 to  $\pi$ . In this way, the echo changes its phase also in  $\pi$ , but the  $\text{FID}_2$  remains unchanged. Changing the receiver phase also from 0 to  $\pi$ , the echoes are added constructively and the  $\text{FID}_2$ s are canceled. This is typically known as the add-subtract phase cycle.

Finally, the third pulse splits the nine pathways generated by the first two pulses into  $3^3 = 27$  paths. From the nine pathways ending in  $q_3 = +1$ , only five can generate a signal [5]. Figure 2.2 shows the paths giving a signal if  $t_2 > t_1$ , and indicates their dependence on the phases of the rf pulses. The first echo in the list is the so-called *direct echo* (DE) formed by magnetization that is always in the transverse plane (defined as direct echo by [1]). The second echo is that formed by the magnetization dephased during the first two evolution periods and rephased during the third one ( $\text{E}_{13}$ ). The third one is the stimulated echo (STE) formed by magnetization that dephases during the first free precession period, is stored as longitudinal magnetization during the second one, and rephases during  $t_3$  after being

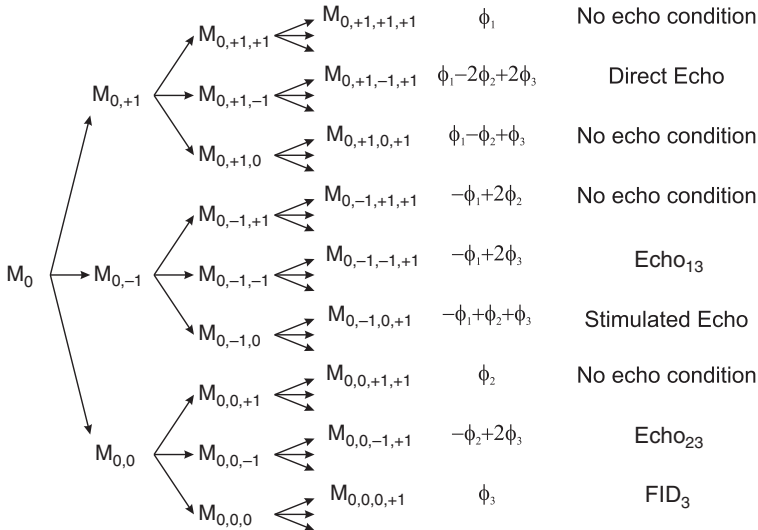


**Fig. 2.2** Coherence pathways generated by the application of three pulses separated by times  $t_1$  and  $t_2$ . Only coherences with  $q_3 = +1$  are shown after the third pulse. From all these potential candidates to generate signal after the third pulse only those fulfilling the echo condition of Eq. (2.12) are listed together with their respective dependence on  $\phi_1$ ,  $\phi_2$ , and  $\phi_3$



**Table 2.1** Phase cycle to select the stimulated echo generated by a three-pulse sequence

$\phi_1$	$\phi_2$	$\phi_3$	$\phi_{DE}$	$\phi_{E_{13}}$	$\phi_{STE}$	$\phi_{E_{23}}$	$\phi_{F3}$	$\phi_{rec}$
0	0	0	0	0	0	0	0	0
$\pi$	0	0	$\pi$	$\pi$	$\pi$	0	0	$\pi$
0	$\pi$	0	0	0	$\pi$	$\pi$	0	$\pi$
$\pi$	$\pi$	0	$\pi$	$\pi$	0	$\pi$	0	0

converted in transverse magnetization by the third pulse. The fourth echo is generated by the magnetization brought to the transverse plane by the second pulse which is refocused after the third pulse ( $E_{23}$ ). The last path describes the signal generated by the third pulse ( $FID_3$ ). Table 2.1 exemplifies the phase cycle needed to select the stimulated echo out of the five interfering signals. It also provides the phase of each signal for each combination of phases chosen for the rf pulses. As the stimulated-echo has to be added constructively, the receiver phase is cycled following the phase shift of this particular pathway. In this way, it can be seen that the other signals are averaged out after the four scans. The selection of other paths can be achieved by changing the phase cycle.

Besides allowing a straightforward identification of interfering signals and simplifying the design of proper phase cycles to disentangle them from the desired pathway, a really powerful advantage of this formalism over the vectorial one described in Sect. 2.1.1 is the possibility to include the effect of diffusion attenuation for each particular pathway. Even though relaxation can be easily included in both formalisms as simple multiplicative factors attenuating the magnetization during the free evolution periods, in order to account for the effect of diffusion we need to know the type of coherence during previous evolution periods to identify if the generated echo has evolved as a direct echo or as a stimulated echo. It is well known that the diffusion attenuation experienced by the direct echo is different from the one experienced by a stimulated echo [5, 11–13]. Thus, each pathway must be weighted by a different diffusion factor. This strategy requires subdivision of a given pathway into segments that form sequences of the form  $(-1, +1)$ ,  $(-1, -1, +1, +1)$ , or higher known as single, double, or higher Hahn echoes and sequences of the form  $(-1, 0, \dots, 0 + 1)$ ,  $(-1, -1, 0, \dots, 0 + 1, +1)$ , or higher, known as single, double, or higher stimulated echoes, respectively. The diffusion attenuation factors for each of these segments can be easily calculated once the type of echo and the timing are defined, hence the total attenuation after  $N$  pulses is just the product of these attenuation factors [4, 10].

Please note that the fresh magnetization created during a free evolution period is not included in this calculation. The new magnetization created during the evolution time  $t_k$  is  $\mathbf{M}^k = (0, 0, 1 - \exp(-t_k/T_1))$  and has to be taken into account only from the  $(k + 1)$ th rf pulse on (see [4]). In most cases, the magnetization created in free evolution intervals set after the first rf pulse is not desired and is eliminated by the add/subtract phase cycle of the first rf pulse (exceptions are sequences used to measure  $T_1$ , where the magnetization created during the evolution period subsequent to the preparation interval is the desired one).

### 2.1.3 Numerical Calculation of the NMR Signal

The NMR signal detected by a given sensor depends exclusively on the geometry of the magnet and surface coil generating the static and rf fields. The strategy to calculate the total signal induced in the coil is based on the subdivision of the object into small voxels where defined  $\mathbf{B}_0$  and  $\mathbf{B}_1$  fields can be assumed. The sequence response is then calculated for every voxel using the rotations defined in the previous sections, and the total signal is obtained as the integration over the volume, weighting the contribution of each voxel by the detection efficiency of the rf coil. This calculation requires the knowledge of the spatial distribution of both fields.

The magnetic field generated by an array of permanent blocks and iron yokes or pole shoes can be calculated by means of finite element methods (FEM). On the other hand, the rf field produced by the rf coil can be obtained by integrating the Biot–Savart equation for the defined coil geometry. This solution does not consider possible distortion of the rf field due to the presence of metallic components in the vicinity of the coil, but it can be applied in most cases. A more exact solution would require the use of finite element calculations also for the rf coil. Once both magnetic field vectors are known at every voxel, the evolution of the magnetization in each voxel can be calculated. As both fields  $\mathbf{B}_0$  and  $\mathbf{B}_1$  may change in magnitude and direction from voxel to voxel, the component of the rf field perpendicular to the static field ( $\mathbf{B}_0$  is assumed to define the local  $z$ -axis in the voxel)

$$(B_1)_{xy} = |\mathbf{B}_0 \times \mathbf{B}_1| / B_0$$

must be used to calculate the effect of the rf pulse at each voxel.

Besides playing a primary role during excitation, the rf coil defines the sensitivity of the sensor to detect the NMR signal from each volume element. This fact leads to a reduction of the contribution from voxels with weak  $(B_1)_{xy}$  in a twofold way. First, just part of the magnetization is brought to the transverse plane and, second, it is detected with less efficiency. The contribution from each voxel to the total signal can be calculated considering that the EMF induced in the rf coil  $C$  by the oscillating magnetization component  $M_{xy}$  placed at  $r$  is, according to the reciprocity principle [14]

$$\xi = -\partial/\partial t \{ (B_1/i)_{xy} M_{xy} \exp(i\omega_0 t) \}, \quad (2.15)$$

where it becomes obvious that the efficiency during the detection of the signal is proportional to  $(B_1)_{xy}$  per unit of current. Then, the total complex signal in the rotating frame can be obtained in arbitrary units by integrating the contribution of the transverse magnetization  $M_{xy} = M_x + iM_y$  at each voxel as

$$S(t) \propto (B_1/i)_{xy} \int_{V_s} M_{xy}(r) dr^3, \quad (2.16)$$

where the components of the magnetization are calculated at the time of the acquisition by applying to the initial magnetization  $\mathbf{M}_0 = (0, 0, 1)$  the rotations describing the pulse sequence.

## 2.2 Pulse Sequence Analysis

The formalism given in the last section allows one to easily calculate the evolution of the magnetization in response to different pulse sequences as a function of both the off-resonance and  $B_1$  inhomogeneity. For simplicity, in this section the analysis is performed by assuming a magnetic field decreasing linearly along the depth and a homogeneous radiofrequency field. In this situation, the frequency distribution is constant, and all frequencies are excited by the same rf amplitude, condition that simplifies the understanding of the off-resonance effect. Then, in those cases where the  $B_1$  inhomogeneity is expected to introduce an appreciable effect, the response is calculated by including in the simulation the field of a surface coil. To emulate one of the most common spatial dependencies found in single-sided sensors, the sample is assumed to be in the presence of a magnetic field  $B_0$  parallel to the surface of the sensor, and it is excited by the rf field generated by a circular single-loop rf coil. For the calculations presented here a coil diameter of 10 mm is used and it is assumed that the on-resonance condition is met 2.5 mm above the coil. Thus the excited planar slice is placed in a region where the rf field is expected to be approximately constant in an area of the size of the coil and then decays quickly as the lateral position increases beyond the radius of the coil. This can be considered as a moderated condition where the rf field is not extremely inhomogeneous.

### 2.2.1 Single rf Pulse

The simplest pulse sequence to be studied is the response to a single rf pulse. Understanding the dynamics of the magnetization under the application of a selective pulse is the key to visualize why off-resonance excitation is an important source of error during most sequences. Figure 2.3a shows the magnetization components after applying a single rectangular rf pulse as a function of the offset  $\Delta\omega_0$ . The simulations were conducted by assuming a homogeneous rf field with an amplitude  $B_1$  such that  $\omega_1 t_p = \gamma B_1 t_p = \pi/2$ , set to define a flip angle of  $90^\circ$  for on-resonance magnetization. It can be observed that, as a consequence of the nutation about a tilted effective field, the magnetization does not necessarily remains on the  $x - z$  plane under the application of an rf pulse along the  $y$ -axis. Figure 2.3b illustrates the position of the magnetization as a function of the offset frequency for an rf pulse applied along the  $y$ -axis.

The magnetization brought to the  $x$ - $y$  plane by the rf pulse, which is a measure of the signal detectable for each frequency, can be calculated as  $M_{xy} = \sqrt{M_x^2 + M_y^2}$ , where  $M_x$  and  $M_y$  are the components plotted in Fig. 2.3a. The amplitude of  $M_{xy}$

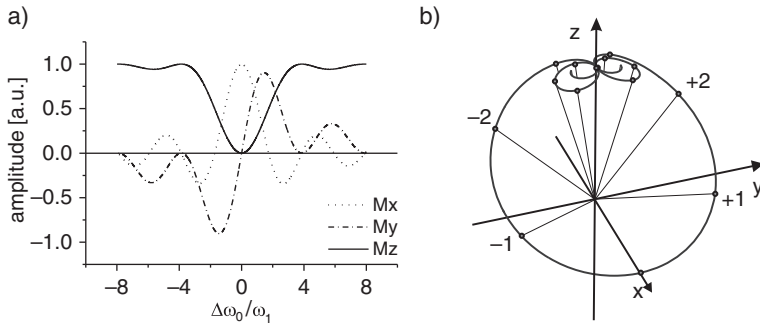


**Fig. 2.3** (a) Magnetization components as a function of the off-resonance after the application of an rf pulse set to define a  $90^\circ$  rotation for on-resonance spins. (b) Orientation of the magnetization vector after the rf pulse as a function of the offset frequency for the rf pulse set in (a). The dots mark the final position of the magnetization vectors for offsets  $\Delta\omega_0/\omega_1 = 0, \pm 1, \dots, \pm 8$

as a function of the offset frequency is plotted in Fig. 2.4a. As it can be observed, full amplitude is obtained up to offset frequencies of the order of the nutation frequency  $\omega_1$ . However, the amplitude quickly decreases for larger offsets showing that efficient excitation can only be achieved in a defined bandwidth. As a rule of thumb, it is usually said that an rf pulse of length  $t_p$  excites a bandwidth  $\Delta\nu_0 = 1/t_p$ . Considering that for a  $90^\circ$  pulse  $\nu_1 = 1/(4t_p)$ , this rule defines a region in Fig. 2.4a between  $\Delta\omega_0/\omega_1 = \pm 2$  (indicated with vertical lines). At the border of this band the magnetization in the transverse plane is  $M_{xy} = 0.8$ . Finally, the dashed line in Fig. 2.4a depicts the sinc function corresponding to the Fourier transform of the rectangular shape of the rf pulse, which predicts the frequency response when working in the linear response limit [8]. Except predicting the position of the nodes, it should be noted that the difference between both curves is not negligible (in particular, in the range marked as the excitation bandwidth of the pulse), a fact that must serve to encourage the reader to use the real spin response for predicting the evolution of the magnetization under defined sequences.

As a consequence of precessing in conical trajectories about effective fields tilted at different angles, not only the magnitude but also the phase of the transverse magnetization varies with the offset. Figure 2.4b shows the phase of the magnetization calculated as  $\phi = \arctan(M_y/M_x)$  as a function of the excitation frequency. It can be observed that  $\phi$  varies almost linearly in the whole range, a fact that will be of extreme importance in the next section at the time of refocusing the magnetization to generate an echo. The spreading of the magnetization on the  $x$ - $y$  plane during the application of the rf pulse leads to important signal attenuation at the end of the pulse. Moreover, as the gradient is continuously present, the magnetization further spreads after the pulse and the signal is averaged out in a free evolution time of the order of the pulse length, which in most cases is of the order of the dead time of the rf probe. Consequently, under typical conditions no FID can be readily detected after applying a selective rf pulse when large samples are in the presence of a static gradient.

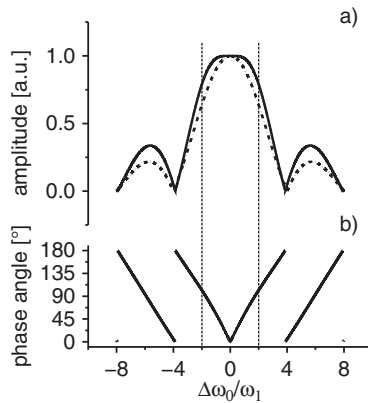


**Fig. 2.4** (a) Magnetization component brought to the plane by the rf pulse plotted as a function of the off-resonance. While a perfect  $90^\circ$  rotation is achieved for on-resonance spins, the efficiency of the excitation quickly decreases with the offset. The vertical lines indicate the bandwidth corresponding to  $1/t_p$ , usually pointed as the excitation bandwidth of a rectangular pulse. (b) Phase of the transverse magnetization. The phase acquired by the magnetization during the pulse is highly linear with the offset frequency, a feature with an important implication at the time of refocusing the spreading during the pulse

### 2.2.2 The Generation of Hahn Echoes

The presence of a distribution of resonance frequencies results in a dephasing of transverse magnetization during and after the application of the rf pulse. The possibility to refocus the phase spreading of the magnetization was discovered by Hahn in 1950 and has become one of the most important realizations for the field of single-sided NMR [5]. The sequence requires the application of a second rf pulse generating a  $180^\circ$  rotation about an axis lying on the  $x$ - $y$  plane. Although in the original work a  $90^\circ$  pulse was used, it was quickly realized that a  $180^\circ$  is needed to efficiently refocus the phase spreading [15]. This rotation inverts the sign of the phase acquired by the magnetization during the time previous to the  $180^\circ$  pulse, leading to its cancelation in a posterior free evolution after the application of the refocusing pulse. Although a free evolution period  $\tau$  is expected to cancel the phase spreading acquired during the time  $\tau$  between the  $90^\circ$  and the  $180^\circ$  pulses, the phase spreading developed during the  $90^\circ$  also needs to be cancelled to acquire full signal. As the phase acquired by the magnetization during the first rf pulse depends almost linearly on the offset, it can be refocused by letting the magnetization evolve an extra time after the application of the inversion pulse. The dephasing during the pulse over a broad frequency range is about the half of the dephasing acquired during free precession, so that the extra time required after the inversion pulse should be about  $t_p/2$ . However, close to on-resonance, the slope of the dephasing curve shown in Fig. 2.4 is slightly larger than the slope defined by half of the offset frequency, requiring a longer delay for magnetization rephasing. If signal coming from

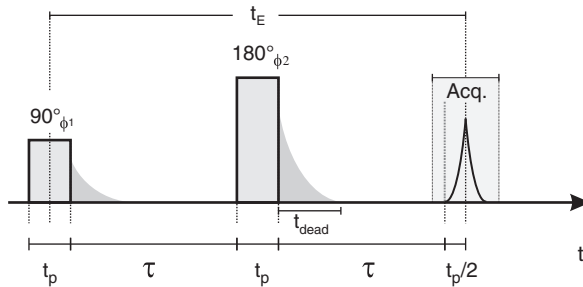


**Fig. 2.5** Hahn echo pulse sequence showing the timing of the pulses and the echo formation

a frequency bandwidth much narrower than the excitation bandwidth of the pulse is going to be retained, the time for optimum refocusing is  $2t_p/\pi$  instead of  $t_p/2$ . This time correction is reported by Hürlimann in [16]. However, as the optimum delay approaches  $t_p/2$  for bandwidths of the order of the excitation bandwidth of the pulse and because minimal sensitivity improvement is achieved with the optimum delay instead of  $t_p/2$ , the later will be used in the following.

Figure 2.5 shows the timing of a Hahn echo sequence, where the echo is generated at a time  $\tau + t_p/2$  after the application of the refocusing pulse. The fact that the dephasing during the first rf pulse is almost half of the one acquired during the same time but under free evolution leads to the definition of zero time for the sequence at the center of the  $90^\circ$  pulse. Then, defining the echo formation as echo time  $t_E$ , the sequence appears symmetric with respect to the center of the  $180^\circ$  pulse. The need for an extra free evolution time after the application of selective pulses used for slice excitation in conventional NMR imaging, which is used to refocus the phase spreading developed during the application of the soft rf pulse [17].

In conventional experiments, where the on-resonance condition is fulfilled,  $180^\circ$  rotations can be well defined. However, as we learned in Sect. 2.2.1, the effect of an rf pulse applied in the presence of a static gradient depends on the resonance offset; a fact that makes impossible to define a  $180^\circ$  rotation for every resonance frequency. The effect of the off-resonance on the refocusing efficiency can be easily calculated assuming a homogeneous  $B_1$  and setting the second rf pulse to define a  $180^\circ$  pulse for the on-resonance spins. At this point, two possibilities are available: either the amplitude of the pulse is doubled keeping its length constant or the amplitude is kept constant and the length is doubled. For the simulations presented in this book we prefer the first option. The total evolution that has to be applied to  $M_0$  to obtain the final state of the magnetization at the time  $t_E$  when the echo is formed can be written as

$$M(t_E) = E(\tau + t_p/2) \rightarrow P(180^\circ, \phi_2) \rightarrow E(\tau) \rightarrow P(90^\circ, \phi_1) \rightarrow M_0. \quad (2.17)$$

Figure 2.6a shows the magnetization at the echo maximum plotted as a function of the offset. It can be observed that the amplitude of the components is modu-

lated by a well-defined frequency. The oscillations appear due to the fact that at the moment when the second pulse is applied, the magnetization is strongly spread in the transverse plane. As the pulse is applied along a particular direction, in this case the  $x$ -axis, those vectors lying along the direction of the rf field at the time when the pulse is applied, remain in the plane untouched, at least for small offsets. However, vectors lying along  $y$ -axis are rotated along the effective field corresponding to the particular offset. For a small offset in the resonance frequency, the rotation is close to be an ideal  $180^\circ$  and the magnetization is placed along the  $y$ -axis after the pulse. However, as the offset increases, the trajectory followed by the magnetization increasingly departs from the ideal one, a fact that leads to the reduction of the component lying in the  $xy$ -plane. Since longer  $\tau$  delays lead to larger phase spread, smaller offsets can complete a rotation about the  $z$ -axis, and the oscillation frequency increases with  $\tau$ . These oscillations cannot be observed in real experiments due to the destructive interference between anti-phase magnetization component at the time of the echo formation. Hence, it becomes necessary to consider in the simulations the fact that in a real experiment signals with different frequencies are detected simultaneously and are thereby subject to strong interference in the time domain. A way to avoid interference would be to use a very thin sample on a magnet generating a uniform gradient along the depth direction, then the signal amplitude for each frequency could be sampled independently to reproduce the result of this simulation.

The numerical tools used up to here to calculate the evolution of the magnetization can be easily applied to calculate the NMR signal generated by the pulse sequence. In contrast to the previous analysis, the calculation of the signal requires knowledge of the real static and rf fields. For the present analysis, a static magnetic field varying linearly along the depth direction and a homogeneous rf field are assumed. In this simplified situation, the real and imaginary signals at a defined time are calculated as the addition of the  $M_x$  and  $M_y$  magnetization components for a large number of offset values lying in a bandwidth much larger than the excitation bandwidth of the rf pulse.

Figure 2.6b compares the magnetization generated along the  $x$ -axis by setting an ideal  $180^\circ$  rotation for every frequency with the one obtained by applying a real rf pulse set to define a  $180^\circ$  rotation for on-resonance spins. Whereas in the first case a spectrum that reproduces the one defined by the first pulse (solid line) is recovered, the resonance offset present during the refocusing pulse yields an oscillatory behavior as a function of frequency (dotted line) that reduces the effective bandwidth measurable in the spectrum obtained as the Fourier transform of the echo signal (dashed line) by a factor of about 2. As the length of the rf pulses defines the excitation bandwidth of the sequence, the echo width is expected to depend on the pulse duration; the longer the pulse is the broader the echo. As a rule of thumb, the echo width is about the pulse length.

Considering that points acquired during the acquisition time can be added to improve the signal-to-noise ratio of the detected echo, the question that arises is how to set the length of the acquisition window to maximize the sensitivity? To answer this question we need to know the shape of the echo for a given  $t_p$ . This analysis

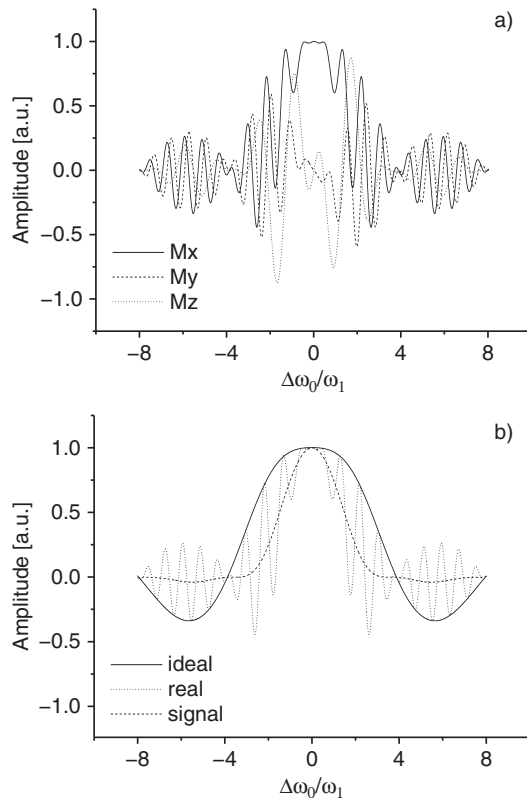


**Fig. 2.6** (a) Magnetization components at the time of the echo formation plotted as a function of the resonance offset. (b) Comparison between the excitation bandwidth of a single rf pulse and the one defined by a Hahn echo sequence

uses the shape of the Hahn echo generated by assuming a uniform distribution of frequencies and a homogeneous rf field. Figure 2.7 shows the signal-to-noise ratio calculated as the addition of the acquired points (total signal) divided by the square root of the number of points added for different acquisition windows (noise). Since the noise power is the same for all points and the signal amplitude decreases when departing from the echo center, maximum sensitivity is obtained when the echo is acquired during a time equal to the length of the rf pulse used for excitation (a more detailed discussion can be found in [8], p. 152).

The timing needed to acquire the echo centered in the acquisition window requires starting acquisition at a time  $\tau + t_p/2 - \text{Acq}/2$  after the application of the  $180^\circ$  pulse, with Acq being the total time to be acquired. However, because the signal is excited and detected by a resonance circuit with a finite bandwidth, a short delay shift (sh) proportional to the quality factor  $Q$  of the circuit is introduced. The value of sh, which must be added to the delay between the second pulse and the acquisition window, needs to be determined for every rf probe, and it can be a few



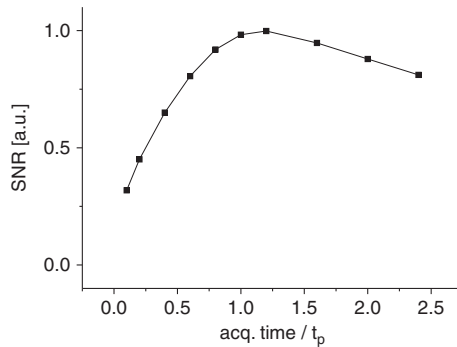


**Fig. 2.7** Signal-to-noise ratio calculated as a function of the acquisition time normalized to the pulse length  $t_p$  for the echo generated by the Hahn echo sequence

microseconds. Under this condition the shortest  $\tau$  that can be reached is determined by the dead time ( $t_{\text{dead}}$ ) of the circuit, the acquisition time, and the pulse length ( $\tau > t_{\text{dead}} + \text{Acq}/2 - t_p/2 - \text{sh}$ ). To shorten the minimum  $\tau$  half of the echo can be acquired by starting the acquisition at the maximum of the echo. Nevertheless, it is achieved at the expense of sensitivity.

The phase of the second pulse influences the phase of the echo, but does not affect the efficiency to refocus the phase spread of the magnetization. In this example we have chosen to apply the  $90^\circ$  pulse along the  $y$ -axis and the  $180^\circ$  pulse along the  $x$ -axis, thereby generating the echo along the  $x$ -axis. A phase cycle of at least two steps (add/subtract) is generally used. It requires applying the  $90^\circ$  pulse first along  $+y$ -axis and then along  $-y$ -axis keeping the phase of the  $180^\circ$  pulse along the  $+x$ -axis in both experiments. Cycling the phase of the first pulse changes the phase of the echo and requires cycling the phase of the receiver from  $+x$  to  $-x$  to constructively add the two signals.

The effect of this phase cycle is twofold. First, it serves to cancel magnetization brought to the transverse plane by an imperfect  $180^\circ$  pulse (path  $M_{0,0,+1}$ ). Second, it cancel spurious signals coming from the dead time of the resonance circuit and possible acoustic ringing generated by the application of the  $180^\circ$  pulse. These unwanted signals are expected to be the same for both experiments because the  $180^\circ$  pulse is applied with the same phase. Thus, as soon as they reach a voltage level that can be digitized by the receiver they are add-subtracted by cycling the phase. It must be noted here that for very short echo times, ringing generated by the first rf pulse might be present at the time the echo is formed. In this case the phase cycle shown in Table 2.2 must be used. This phase cycle eliminates both the signal generated by the first pulse (path  $M_{0,+1,+1}$ ), which for short echo times may still be present in systems with a small static gradient, and the ringing generated also by this rf pulse.

The Hahn echo sequence is of particular interest to measure extremely short relaxation times of the order of a few dead times of the resonance circuit, a situation where multi-echo techniques can only generate a few echoes and are inaccurate to determine the  $T_2$  of the sample. Although resonance offset leads to a distribution

**Table 2.2** Phase cycle to select the Hahn echo filtering the signals of the first and second rf pulses as well as acoustic ringing present after the pulses

$\phi_1$	$\phi_2$	$\phi_{\text{rec}}$
$+\pi/2$	0	0
$-\pi/2$	0	$\pi$
$+\pi/2$	$+\pi/2$	$\pi$
$-\pi/2$	$+\pi/2$	0

of flip angles across the sample, the magnetization generating the echo evolves as transverse magnetization during the whole sequence and decays purely with  $T_2$  (no  $T_1$  contamination is present as in the case of the CPMG decay). In this case, the application of imperfect rotations to refocus the phase spread introduced by the field inhomogeneities do not affect the characteristic time decay measured by the sequence, which is expected to be the same as the one measured in homogeneous fields. A exception is for the case of liquids measured in a strong gradient. In this case, the echo amplitude is also attenuated by the self-diffusion of the molecules in the presence of the static gradient. In the case of unrestricted Brownian motion, this attenuation is

$$S(t_E) = S_0 \exp \left( -\frac{t_E}{T_2} - \frac{1}{12} \gamma^2 G_0^2 D (t_E)^3 \right). \quad (2.18)$$

For sensors generating a uniform static gradient, the Hahn echo sequence is a very sensitive method to measure diffusion coefficients. Since gradients generated by single-sided sensors are very strong, they can be used to measure very small diffusion coefficients. Moreover, the Hahn echo sequence has been extensively used in low-field NMR to study polymers, where the echo decay is usually fitted by a number of exponentials or even the addition of exponential and gaussian functions.

### 2.2.3 The CPMG Sequence

The success of single-sided sensors mainly relies on the extraordinarily good performance of multi-echo sequences that successively refocus the phase spread due to the static field inhomogeneities and lead to the generation of echo trains. For most samples, the minimum echo time that can be set in a Hahn echo sequence is much shorter than  $T_2$ , and a large number of echoes can be generated by applying a train of refocusing pulses with the right phase. It was first Carr and Purcell [6] who proposed the use of repeated refocusing to measure  $T_2$  in a single shot. However, as the original sequence uses refocusing pulses with the same phase as the first pulse, it suffers from accumulative distortions due to slight errors in the definition of the flip angle of the refocusing pulses. A modification to the CP sequence, proposed later by Meiboom and Gill [7], is known as the CPMG sequence. The timing of the pulse sequence is depicted in Fig. 2.8.

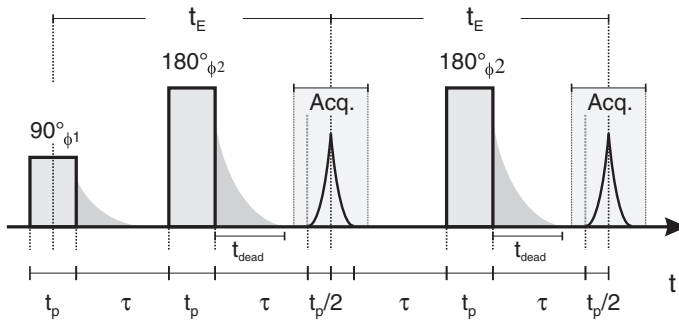


**Fig. 2.8** Carr-Purcell-Meiboom-Gill pulse sequence. A  $90^\circ$  phase shift between the first pulse and the train of  $180^\circ$  pulses eliminates accumulative distortions introduced by imperfection of the rf pulse and resonance offset. The time between the first two pulses is not exactly half the time between  $180^\circ$  pulses, but  $t_p/2$  shorter. As discussed in Sect. 2.2.2, the sensitivity can be improved by varying this extra delay time [16], but  $t_p/2$  can be used with similar performance

The modification introduced by Meiboom and Gill consists of shifting the phase of the refocusing train by  $90^\circ$  with respect to the first pulse. By doing so the distortions coming from the mentioned imperfections are strongly reduced. The sequence is so robust that it can be implemented in strongly inhomogeneous fields with outstanding performance. Figure 2.9 shows the behavior of the first echoes generated by this sequence. For this calculation, an echo time  $t_E = 0.2$  ms, rf pulses of  $10 \mu\text{s}$ , and infinite  $T_1$  and  $T_2$  were assumed. After a transient of three echoes, the signal amplitude remains constant showing that the field inhomogeneities do not lead to a signal loss as in the case of the CP sequence. The CPMG sequence is, in general, implemented using a simple add-subtract phase cycle. It requires cycling  $\phi_1$  and the receiver phase from  $0$  to  $\pi$  keeping  $\phi_2$  unchanged.

The dynamics of the magnetization during the CPMG sequence have been extensively studied in the past [1–3]. Different authors have demonstrated that the echo signals detected during this echo train are complicated superposition of coherence pathways where the magnetization stays alternatively along the longitudinal direction or in the transverse plane. Whereas, for example, the first echo is formed by magnetization that evolved only in the transverse plane (pathway  $M_{0,-1,+1}$ ), the second echo is the superposition of signal that was in the plane (direct echo) plus the stimulated echo generated by magnetization stored along the  $z$ -axis by the first  $180^\circ$  pulse and brought back to the transverse plane by the second pulse (pathways  $M_{0,+1,-1,+1}$  and  $M_{0,-1,0,+1}$ , respectively). As the echo number increases, the number of pathways contributing to the echoes also does it. In strongly inhomogeneous fields, this superposition of pathways quickly reaches a steady state and after three or four echoes the signal amplitude remains constant (in absence of relaxation). The typical behavior shows that the amplitude of the first echo is the smallest and that of the second is the largest. Then, subsequent echoes reach a steady state.

This behavior can also be observed by calculating the bandwidth of each echo. Figure 2.10 compares the excitation bandwidth of a single pulse, shown as a

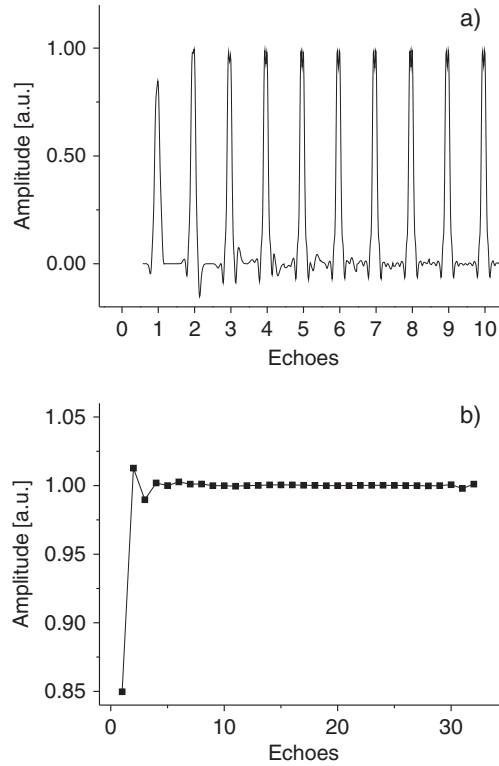


**Fig. 2.9** (a) First echoes generated by the CPMG sequence. Like in the previous section the rf field was assumed to be homogeneous and the signal was calculated as the addition of 2500 signals for frequencies distributed in a bandwidth of  $\pm 2/t_p$ . The number of frequencies used to discretize the frequency bandwidth depends on the total time  $T$  of the sequence. As a rule of thumb the total bandwidth must be divided by a frequency step  $1/T$ . (b) Echo amplitudes obtained by integration of the echo during a time  $t_p$

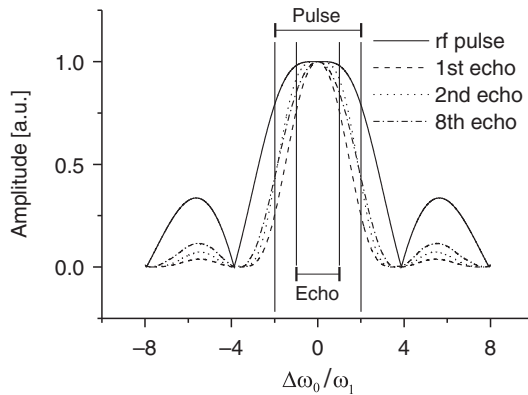


**Fig. 2.10** Excitation bandwidth for different echoes of a CPMG sequence. The bandwidth of a single pulse is shown for reference. Whereas the first echo has a bandwidth of about half of that of a single pulse, thanks to the mixture of coherence pathways, the steady-state echo bandwidth is slightly broader than the one of the first echo (Hahn echo)

reference, with that of the first, the second, and the eighth echo. The bandwidth of the first echo is clearly the narrowest. Then, it increases to a maximum for the second echo due to the superposition of the direct echo with the stimulated echo. Thereafter, it slightly decreases to reach the steady state. In this case, the spectra were obtained as the Fourier transforms of the echo signals shown in Fig. 2.9. The transient depends on the  $B_0$  and  $B_1$  distributions and the acquisition bandwidth. For an acquisition window set longer than the pulse length, off-resonance signals can be filtered, and almost no oscillation in the first echoes is observed. The amplitudes of the transient can be determined theoretically or experimentally to be used later as a calibration for correcting the data before numerical analysis.

An important consequence of the mixture of different coherence pathways comes from the fact that magnetization stored along the  $z$ -axis relaxes with  $T_1$ , while magnetization that remains on the plane relaxes with  $T_2$ . This leads to an effective echo train decay time  $T_{2\text{eff}}$ , which is a mixture of  $T_1$  and  $T_2$ , instead of only  $T_2$  [1]. The effective time decay is directly obtained from the simulations by including the attenuation factors  $e_1(\tau)$  and  $e_2(\tau)$  in the rotation matrix of the free evolution (Eq. 2.6). The increasing superposition of coherence pathways leads to a signal decay that departs from a single exponential decay. Figure 2.11 shows the results of numerical simulations assuming  $T_1 = T_2$  and  $T_1 = 6T_2$ . The calculations were done by assuming first a homogeneous  $B_1$  field and then including the real rf field generated by a surface coil (inhomogeneous  $B_1$ ). As expected, for  $T_1 = T_2$  an exponential signal decay is obtained, but for  $T_1 = 6T_2$  the superposition of pathways leads to a non-exponential decay that is apparent for sufficiently long times. When a inhomogeneous rf field is included in the simulations the mixture of coherence

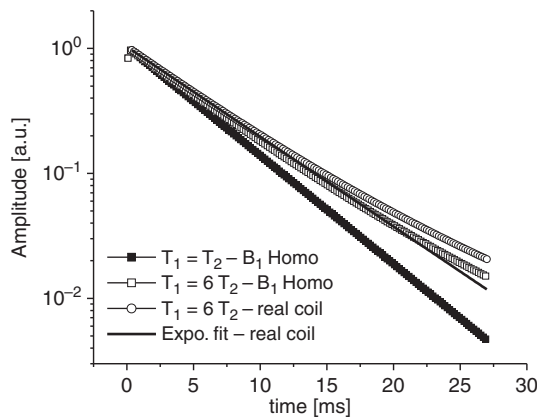


**Fig. 2.11** Signal decay during a CPMG sequence calculated for  $T_1 = T_2 = 5$  ms and  $T_1 = 6$ ,  $T_2 = 30$  ms. The simulations used the following parameters,  $t_E = 100 \mu\text{s}$ ,  $t_p = 10 \mu\text{s}$ , acquisition bandwidth equal to the excitation bandwidth of the rf pulse ( $1/t_p = 100$  kHz), and  $N_{\text{echoes}} = 300$ . It can be observed how the  $T_1$  contamination influences the value of the slope ( $T_{2\text{eff}}$ ) and defines a non-exponential decay. The presence of an inhomogeneous  $B_1$  field, included in the simulation by integrating over a plane  $15 \times 15 \text{ mm}^2$  at 2.5 mm above a circular loop with 10 mm in diameter, does not lead to appreciable enhancement of  $T_1$  contamination compared to the result obtained for a homogeneous  $B_1$  field. The fitting shows that the a single exponential can fit well the data if the decay is considered up to one-third

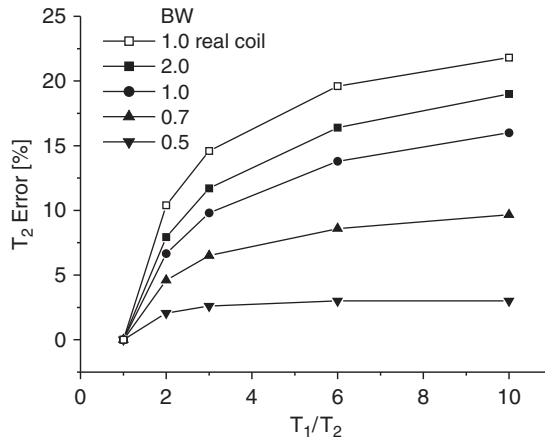


**Fig. 2.12** Deviation of the decay time of the echo train generated by a CPMG sequence simulated as a function of the  $T_1/T_2$  ratio and for different detection bandwidths. The decay times were obtained by fitting the signal decays up to one-third of its initial amplitude (one  $T_2$ ). The deviation obtained in the presence of the inhomogeneous  $B_1$ -field generated by the surface coil was calculated only for an acquisition bandwidth matching the excitation bandwidth, condition where maximum sensitivity is expected. The simulations were done assuming the parameters listed in Fig. 2.11

pathways is larger. However, only a slightly longer  $T_{2\text{eff}}$  is obtained. In practice, the signal decay can be well fitted to a single exponential if a maximum time of the order of  $T_2$  is considered, which is the case even in the presence of an inhomogeneous  $B_1$  field (Expo. fit in Fig. 2.11).

As shown by Goelman and Prammer [1], the error in measuring  $T_2$  via a CPMG sequence depends on the  $T_1/T_2$  ratio and on the bandwidth used for the detection, which should be measured as a fraction of the excitation bandwidth. The dependence of the error on these parameters is illustrated in Fig. 2.12. Although the error is zero only when  $T_1=T_2$ , the only situation when  $T_{2\text{eff}}$  is equal to  $T_2$ , the error grows as the ratio  $T_1/T_2$  increases. As explained previously, the mixture between  $T_2$  and  $T_1$  is due to the off-resonance excitation. In this way, by reducing the detection bandwidth the mixture is expected to decrease. This dependence is clearly observed in Fig. 2.12, where the error was calculated as a function of the ratio  $T_1/T_2$ , for different bandwidths measured proportional to the bandwidth of the rf pulse. In the last section we have shown that maximum sensitivity is achieved when the acquisition bandwidth is set equal to the excitation bandwidth (Fig. 2.7). It is observed that when setting the detection bandwidth to achieve maximum sensitivity, the error in measuring  $T_2$  remains lower than 15% even for a  $T_1$  10 times longer than  $T_2$ .

These simulations were conducted assuming a homogeneous  $B_1$  field, but this is not the situation found in real sensors. In the presence of an inhomogeneous radiofrequency field, even on-resonance magnetization is spread to coherence pathways that include evolution periods when it is stored along the longitudinal axis and is contaminated by  $T_1$ . Figure 2.12 shows the error in the  $T_2$  measurement obtained

when a surface rf coil is used for excitation and detection. In this case, the acquisition window was set to match the acquisition bandwidth with the bandwidth of the rf pulse. Although the error is larger than the one obtained for a homogeneous  $B_1$  field, it is still about 20% for a  $T_1$  10 times longer than  $T_2$ . This confirms that the CPMG sequence can be used to measure the transverse relaxation time even in the presence of a strong static gradient excited with an inhomogeneous  $B_1$  field.

When the CPMG sequence is applied to measure the relaxation time of liquids in the presence of a static gradient, the signal decay is attenuated by molecular Brownian displacement. In slightly inhomogeneous fields, where only direct echoes contribute to the signal, the characteristic time decay of the echoes is given by

$$S(mt_E) = A \exp\{-(1/T_2 + 1/12(\gamma G_0 t_E)^2 D)mt_E\}. \quad (2.19)$$

This equation shows that in the presence of molecular self-diffusion, the signal decay measured by a CPMG sequence is shortened depending on the strength of the static gradient. A way to reduce this distortion is to reduce the echo time  $t_E$ , but this is a realistic solution only up to certain limit. Whereas for a gradient of 1 T/m, an echo time of 0.1 ms suffices to measure a  $T_2$  of about 1 s with an error of 10%, in a gradient of 20 T/m, a time decay of about 20 ms would be measured for this echo time. Actually, for off-resonance excitation the equation given above is not valid anymore and the particular attenuation of each of the many coherent pathways contributing to the signal must be calculated considering their particular time dependencies.

The effect of diffusion during a CPMG was considered by Goelman and Prammer [1] who separated the signal into direct and indirect echoes and calculated expressions for the first three echoes. Later Hürlimann presented a formalism that decomposed the signal into different pathways and calculated the diffusion decay for the first 15 echoes, where he estimated a superposition of  $10^6$  pathways. Finally, a formalism that allows the incorporation of diffusion attenuation for the complete echo train was presented by Song [10], who classified the coherence pathways and showed that only a fraction of the total number of pathways significantly contributes to the signal. He observed that long pathways can be decomposed into a combination of short segments like stimulated  $(-1,0,+1)$  and spin echoes  $(-1,+1)$ . Using this approach, he demonstrated that direct and stimulated echoes contribute to 95% of the CPMG echo signal, thereby showing that despite the large variety of contributing pathways, the final behavior remains simple.

For material characterization, numbers need to be derived from the echo envelope decay (Fig. 2.11). These numbers can be obtained either from a fit of the experimental data with a model function or by calculating a relaxation weight similar to spin echo imaging, for example,  $S(t_1)/S_0$ . In the case of exponential relaxation, the fit parameters are the amplitude  $S_0 = S(t = 0)$  corresponding to the number of spins in the sensitive volume and the relaxation time  $T_{2\text{eff}}$ . But usually the decay is not mono-exponential. A good empirical fit function is the scaled stretched exponential function  $S(t) = S_0 \exp(-(t/T_{2\text{eff}})^b/b)$ , where the factor  $1/b$  has been introduced

to arrive at an exponential function for  $b = 1$  and a Gaussian function for  $b = 2$ . If a bi-exponential function with a long relaxation time  $T_{2\text{eff,long}}$  and a short relaxation time  $T_{2\text{eff,short}}$  is fitted with this function,  $T_{2\text{eff}}$  is close to  $T_{2\text{eff,long}}$ , which from experience is the relaxation time which varies more strongly with the material properties. Compared to the bi-exponential function this stretched exponential function has one less fit parameter and therefore provides a more reproducible fit in the presence of noise-contaminated signals. Before the CPMG decay is fitted, the first echoes must be corrected for the transient effect. This characteristic oscillation can be extracted by measuring a sample with long  $T_2$  or they can be simply eliminated if a large number of echoes are available.

Instead of fitting the experimental data with a model function, they can be transformed for analysis. A useful transformation is the regularized inverse Laplace transformation which transforms the echo envelope into a distribution of relaxation times. This approach is routinely used in well logging, where relaxation time spectra are interpreted in terms of hydrocarbon content, viscosity of fluids in porous rocks, and pore-size distribution [18]. Alternatively, the initial amplitude of the echo envelope can be diffusion encoded, and 2D data sets be measured and transformed into correlation and exchange maps of distributions of relaxation times and diffusion coefficients [19, 20]. Similar to 2D spectroscopy, this approach is useful in separating the contributions to the relaxation time distribution in multi-component systems such as oil and water in well logging. This approach is described in detail in Chap. 3.

When a CPMG sequence is implemented on a real sensor two parameters must be set carefully, the optimum rf pulse duration and the minimum echo time. In a numerical simulation the pulse amplitude or length can be easily set to define a desired flip angle in a defined voxel. However, in a real experiment, where the measured signal amplitude is a value averaged over the sensitive volume, this is not an option. The criterium adopted in this case to set the pulse length is simply the maximization of the signal amplitude. Figure 2.13 shows the dependence of the signal amplitude with the rf strength for both a homogeneous rf field and the field distribution generated by a surface coil. For a homogeneous  $B_1$  field the maximum signal is obtained when the rf amplitude is set to define a rotation slightly larger than  $90^\circ$  for on-resonance spins; however, in the presence of a  $B_1$  distribution this value is generally larger. In the present simulation, where a single loop is used to excite the spins at a depth defined at half of its radius, the maximum is obtained when the strength in the center is about 20% larger than the one needed to define the  $90^\circ$  rotation for on-resonance spins. Thus, the maximum signal is obtained when the optimal rotation is defined for spins lying away from the coil axis. The position of the maximum depends on the rf field distribution generated by the rf coil, which even for the same coil is expected to vary when a different working depth is set.

Regarding the echo time to be set in a CPMG sequence, it has to be noted that to maximize the sensitivity, the maximum number of echoes has to be generated during the echo train. It is achieved by setting the shortest echo time without signal contamination resulting from dead time. It can be found simply by setting an acquisition time shorter than the echo width to ensure that signal is present at all acquired points. Then, the echo time is reduced until the first acquired point becomes distorted. This



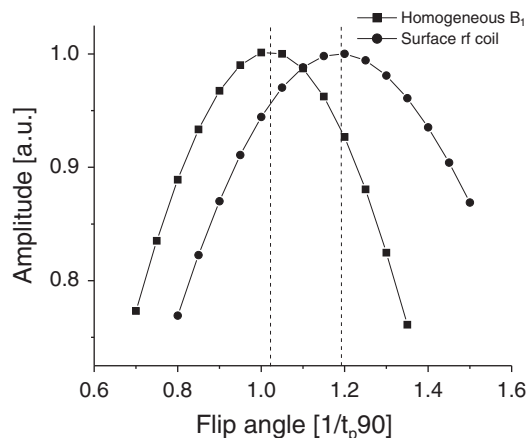


**Fig. 2.13** Signal amplitude detected in a CPMG sequence calculated as a function of the strength of the rf pulses. The rf strength is normalized in the plot to the one required to define a  $90^\circ$  rotation (for the first pulse) for on-resonance spins. In the case of a homogeneous  $B_1$  the maximum is obtained for an rf strength only 5% larger than the optimal one. However, for a real coil the maximum signal is achieved when the strength is 20% larger than that required to define a  $90^\circ$  rotation for on-resonance spins in the axis of the coil. The maximum of the distribution is achieved when the optimal flip angle is defined for spins lying at a certain radius from the coil axis where the rf strength is smaller. The position of the maximum strongly depends on the coil geometry, distance to the coil, and detection bandwidth. For this simulation, the field of a single circular loop 10 mm in diameter was calculated at a depth of 2.5 mm, and the detection bandwidth was matched to the excitation bandwidth of the pulses

is the evidence that the dead time is longer than the delay between the  $180^\circ$  pulses and the acquisition windows. The minimum echo time is the shortest one without signal distortion.

### 2.2.4 Inversion and Saturation Recovery

The spin-lattice relaxation time  $T_1$  is the characteristic time needed by the spin system to exchange energy with its surrounding (the “lattice”). Pulse sequences designed to measure  $T_1$  consist mainly of three stages: (i) a first preparation period during which one or more rf pulses are applied to modify the longitudinal magnetization of the system, taking it away from its equilibrium state, (ii) a free evolution period when the spin system is allowed to relax to the equilibrium state, and (iii) a detection period when the state of the system is measured by converting the longitudinal magnetization into transverse magnetization. The measurement requires a 2D experiment in which the duration of the evolution interval is varied to cover a time range of the order of several  $T_1$ s.

Figure 2.14 shows the two main alternative pulse sequences known as inversion recovery [21] and saturation recovery [22], which are adapted for use in

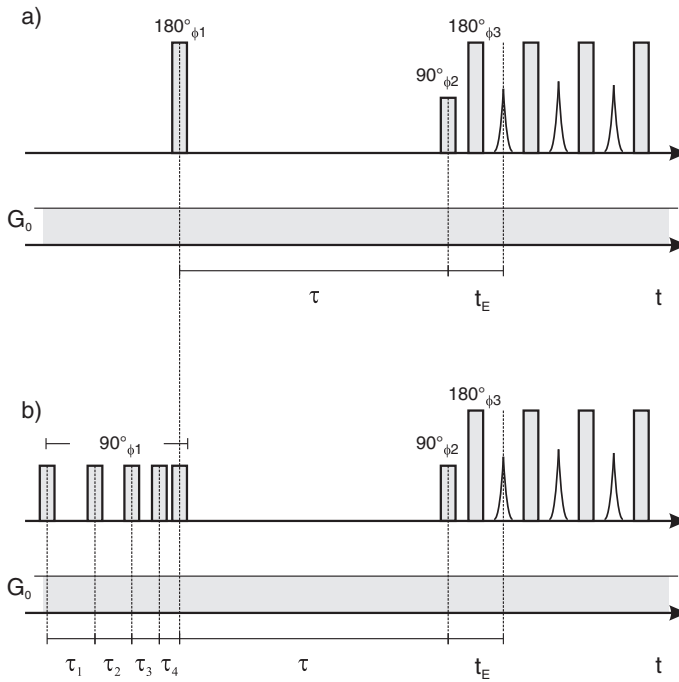


**Fig. 2.14** Inversion- (a) and saturation-recovery (b) pulse sequences adapted to measure the spin-lattice relaxation time  $T_1$  in inhomogeneous fields

inhomogeneous magnetic fields. Implementing these pulse sequences in inhomogeneous fields is difficult mainly because it is impossible to achieve full magnetization inversion or saturation across the full sample. A detailed description of this problem is presented below. It should also be noted here that instead of the single  $90^\circ$  pulse typically used in the detection period to excite an FID, a CPMG sequence is implemented to generate a long echo train that can be co-added to improve sensitivity.

In homogeneous  $B_0$  and  $B_1$  fields, the inversion-recovery sequence uses a hard  $180^\circ$  pulse in the preparation period to invert the equilibrium magnetization  $M_0$  from  $z$  to  $-z$ . Under this ideal condition, the magnetization recovers during the free evolution period  $\tau$  as  $M(\tau) = M_0(1 - 2e^{-\tau/T_1})$ . This result is actually the addition of two contributions: one being the magnetization stored along  $-z$ -axis by the inversion pulse that decays as  $M(\tau) = M_0e^{-\tau/T_1}$  (described by the pathway  $M_{0,0,-1,+1}$ ), and the second, the fresh magnetization created during the evolution time  $\tau$  that grows as  $M(\tau) = M_0(1 - e^{-\tau/T_1})$  (described by the pathway  $M_{0,0,-1,+1}^1$ ). However, as described in Sect. 2.2.1, rf pulses act only in a finite bandwidth defined by the pulse length  $t_p$ , so their performance strongly depends on the off-resonance frequency (see Fig. 2.3). In this way, when the  $180^\circ$  pulse is applied in the presence of a strong static gradient, it cannot invert the magnetization over the whole frequency range across the object.

As a consequence of the partial inversion defined by the  $180^\circ$  pulse, the magnetization at  $\tau = 0$  is not  $-M_0$ , but just a fraction of it. If  $M_{\max}$  is the maximum magnetization detected during the CPMG sequence (detection period) in a certain bandwidth and for long evolution times, it is observed that the measurable magnetization at  $M(\tau = 0)$  depends on the frequency bandwidth. For example, if just a very narrow portion of the spectrum close to the on-resonance condition is integrated, the initial magnetization can be made  $-M_{\max}$  (if  $B_1$  is assumed to be homogeneous). However, this is not a practical solution in terms of sensitivity because just a very small fraction of the total excited spins is detected. If the signal is integrated over a bandwidth  $1/t_p$  for optimum sensitivity (see Fig. 2.7), the initial value is about  $-M_{\max}/2$  (Fig. 2.15a). Thus, the dynamic range reduction of the  $T_1$  curve,

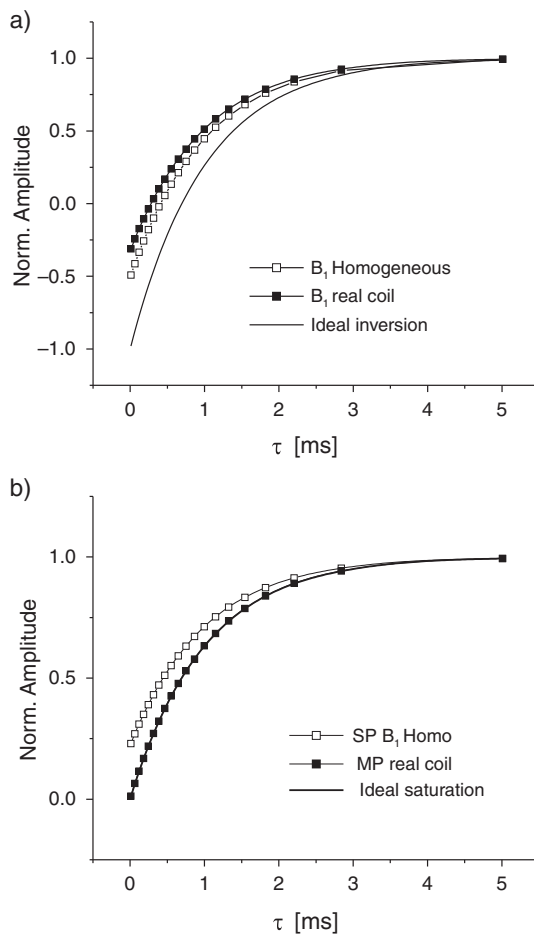


**Fig. 2.15**  $T_1$  buildup curves measured by the inversion- (a) and saturation-recovery pulse sequence (b) in inhomogeneous magnetic fields. The curves are normalized to  $M_{\max}$

which is more pronounced in the presence of an inhomogeneous  $B_1$  field (Fig. 2.15a), reduces the accuracy of the  $T_1$  determination, but does not lead to the measurement of a wrong relaxation time.

A further complication observed when implementing the sequence in inhomogeneous fields arises from the fact that the flip angle distribution generated by the inversion pulse leaves considerable transverse magnetization that may interfere during the detection period with the coherence pathways encoding the  $T_1$  information. To filter these spurious signals, a proper phase cycle is needed. As the pathways evolving as transverse magnetization during the evolution period depend on the phase of the inversion pulse, but those of interest for an inversion-recovery measurement ( $M_{0,0,-1,+1}$  and  $M_{0,0,-1,+1}^1$  describing the magnetization inverted by the first pulse and the fresh magnetization created during the evolution period, respectively) do not, the unwanted ones can be eliminated by cycling the phase of the inversion pulse by  $180^\circ$  while keeping the receiver phase constant. Combining these two steps with the typical add/subtract phase cycle for the  $90^\circ$  pulse of the CPMG sequence applied during the detection period (needed to cancel the signal after the  $180^\circ$  pulses) leads to the four-step loop shown in Table 2.3. Although the phase of the inversion pulse does not need to be synchronized with the phases of the pulses applied in the CPMG sequence, it is interesting to note that if the inversion pulse and the  $90^\circ$  pulse of the CPMG are applied along the same axis, the spurious signals are generated in quadrature to the desired signal. The possibility to separate these two signals allows one to eliminate the phase cycle for the inversion pulse. Then, in cases where the sensitivity of a single scan is acceptable and short experimental times are mandatory, a single phase step can be used if the signal after the  $180^\circ$  pulses of the CPMG is averaged out by dephasing in the presence of the static gradient (a condition that is fulfilled in strongly inhomogeneous fields if rf pulses are shorter than the dead time). In this way, just by setting the receiver phase in a conventional CPMG sequence to detect the echoes on the real channel would ensure that when using the first step in Table 2.3 the coherence pathway encoding the  $T_1$  information will generate signal only in the real channel and the unwanted ones will contribute to the imaginary one.

To measure a  $T_1$  buildup curve, a series of experiments is repeated varying the delay  $\tau$ . Considering that the function to be sampled is expected to be an exponential (at least for liquid-like samples) it is convenient to vary  $\tau$  logarithmically. This guarantees that the buildup curve is sampled at constant amplitude steps, setting more points at short times, where the curve varies with the largest rate, and less points at the end, where almost no variation is expected. Moreover, as experiments

**Table 2.3** Phase cycle for the inversion- and saturation-recovery pulse sequences

$\phi_1$	$\phi_2$	$\phi_3$	$\phi_{\text{rec}}$
0	0	$\pi/2$	0
$\pi$	0	$\pi/2$	0
0	$\pi$	$\pi/2$	$\pi$
$\pi$	$\pi$	$\pi/2$	$\pi$

with longer  $\tau$  are more time consuming to measure, this sampling strategy leads to a reduction in the experimental time. If  $\tau$  is set to vary up to  $5T_1$  the time steps can be calculated as

$$\tau_i = -T_1 \ln \left( 1 - \frac{(1 - \exp(-5))}{(N_{\text{pts}} - 1)} \times i \right), \quad (2.20)$$

where it is assumed that the function  $e^{-\tau/T_1}$  varies from 1 to  $\exp(-5)$ , and  $N_{\text{pts}}$  is the number of points to be measured in the  $T_1$  curve. As the magnetization is affected during the detection period, a recycle delay of at least  $5 T_1$  must be included between experiments in order to ensure that the system is in equilibrium before the next experiment starts. A wrong setting of the recycling delay would lead to a smaller initial magnetization (distorting the  $T_1$  curve), requiring a good guess of  $T_1$  before it can actually be measured. This fact leads to time-consuming overestimations. It can be calculated that the measurement time to complete an inversion-recovery experiment is  $7.5 \times T_1 \times N_{\text{pts}}$  for a linear  $\tau$  increment, and  $6 \times T_1 \times N_{\text{pts}}$  for a logarithmic one.

Another variant used to measure  $T_1$  is the saturation-recovery pulse sequence [22]. In homogeneous fields it uses a first  $90^\circ$  pulse to saturate the magnetization instead of inverting it, consequently, during the evolution period  $\tau$  the longitudinal magnetization grows from zero to its equilibrium value  $M_0$  with the time-dependence  $M(\tau) = M_0(1 - e^{-\tau/T_1})$ . As this sequence starts nullifying the longitudinal magnetization, it does not require any recycle delay in between experiments. This not only leads to a considerable shortening of the measurement time, but it also eliminates the need to know in advance an estimation of the  $T_1$  of the sample. In other words, a wrong setting of the time range for  $\tau$  just leads to sample the buildup curve in a non-optimal way. Nonetheless, the characteristic time extracted from the fit is the correct one (just a poorer accuracy is expected from the experiment because the signal variation does not cover the full dynamic range).

When the sequence is implemented in an inhomogeneous magnetic field, saturation is only achieved for the on-resonance spins (assuming a homogeneous  $B_1$  field), but just partial saturation is achieved for off-resonance ones. Consequently, some remnant magnetization stays along the  $z$ -axis after the saturation period. Hence, the  $T_1$  curve at  $\tau = 0$  starts from an offset value, which, for a detection bandwidth matched to the bandwidth of the pulse, is about 1/4 of the maximum signal measured for  $\tau \gg T_1$ . To visualize the offset, a  $T_1$  measurement was simulated by assuming the system is in equilibrium before the next saturation pulse is applied (Fig. 2.15b). Experimentally this condition is fulfilled by including a long recycle delay between scans. As for the inversion-recovery sequence, the  $T_1$  extracted from this buildup curve is the exact one, without being distorted by the off-resonance effects. However, in the real experiment, where no recycle delay is used, the situation is more complicated because the offset signal measured in a given scan depends on the longitudinal magnetization at the end of the previous one. The remnant magnetization at the end of one measurement is determined by both the evolution time and the saturation effect of the detection period during this scan. Whereas single

Hahn echo detection may leave considerable longitudinal magnetization, a long CPMG echo train can act as an effective saturation period. Then, the offset would be present in the first scan, but already the second scan would show a negligible offset thanks to the saturation provided by the CPMG detection of the previous scan. Important improvement can be achieved when the  $T_1$  curve is sampled in an inverse way, starting from the long  $\tau$  values. Then, if the first point is measured for a recovery time  $\tau \gg T_1$ , the value measured is close to  $M_0$  and is independent of the offset left after the saturation. When  $\tau$  is shortened to measure the second point, the pre-saturation achieved by the first scans reduces the longitudinal magnetization, attenuating the offset by a considerable factor.

Even though a CPMG detection combined with inverse sampling of the evolution times can considerably reduce the offset in the curve, it must be noted here that the measurement of a given point depends on the efficiency of previous scans to saturate the magnetization, which also depends on the  $B_1$  homogeneity. Moreover, it must be pointed out that the recycle delay between scans is not a precise delay and it may depend on interruptions of the spectrometer between experiments. If this happens, unexpected recovery of the magnetization can induce a larger offset in the measured point. A way to improve decoupling between scans uses multiple  $90^\circ$  pulses applied at irregular times in order to achieve more efficient saturation during the preparation period (see Fig. 2.14b). Optimum performance is achieved by applying an odd number of  $90^\circ$  pulses separated by increasing time delays longer than the  $T_2^*$  of the FID. In this way, the natural inhomogeneity of the magnet is used as crusher gradient to spoil the magnetization in between pulses. In addition to the mixing achieved by resonance offset, the fact that the rf field is also inhomogeneous leads to a more efficient cancelation of the magnetization. This is true, because during the train of saturation pulses the magnetization across the sample nutates with different frequency. This spreading defined by the inhomogeneous  $B_1$  field is efficient to mix even on-resonance magnetization.

This approach is useful for magnets with poor homogeneity and becomes very efficient in single-sided systems, where really short delays between pulses of the order of the rf pulse length are enough to strongly mix magnetization components. It should be noted that at the end of the saturation period, the longitudinal magnetization is not zero for each frequency, but it quickly oscillates from positive to negative values as a function of the resonance offset. The anti-phase longitudinal magnetization created during the preparation period gives no signal when it is brought to the transverse plane during the detection period. Thus, only the magnetization recovered during the evolution period is expected to contribute to the signal. Using multi-pulse saturation and inverse sampling, a full dynamic range of the magnetization (from 0 to  $M_0$ ) is obtained even in inhomogeneous fields. The simulations shown in Fig. 2.15b were performed using the  $B_1$  field generated by a surface coil, indicating that the good performance of the sequence is not affected by the presence of radiofrequency inhomogeneity. It must be mentioned that to reduce the offset, the delays between pulses may require small adjustment depending on the sensor where it is implemented in order to achieve the cancelation of the longitudinal magnetization stored in anti-phase (same positive and negative magnetization stored along the

$z$ -axis). In spectrometers with rf modulation capabilities more complicated schemes based on the use of soft pulses or frequency sweeps can be implemented to improve the degree of saturation.

Finally, the important fraction of magnetization brought to the transverse plane by the saturation pulses applied during the preparation period of this sequence needs to be canceled to avoid interference with the magnetization created during the evolution time  $\tau$ , which is brought to the plane during the detection period. In contrast to the inversion-recovery sequence, even working under ideal conditions, full magnetization is left in the transverse plane by the preparation period. A simple solution implemented in systems equipped with gradient coils uses a crusher gradient to spoil the residual magnetization right after the saturation pulses. Although in inhomogeneous fields the background gradient acts also as a spoil gradient during the evolution period, the same gradient is present during the detection period when refocusing pulses are applied. Then, under certain conditions (evolution time shorter than the duration of the detection sequence), the magnetization spread out during the evolution period is refocused and may interfere with the desired magnetization encoding the  $T_1$  information. The same phase cycle described for the inversion recovery sequence removes the signal coming from this non-desired coherence pathways, but its use requires similar magnetization before the saturation period for all the scans involved in the phase cycle loop. This condition is satisfied up to certain point when the  $T_1$  curve is sampled in an inverse way (from long to short  $\tau$  values) and the longest  $\tau$  is larger than  $T_1$ . It is interesting to note that applying the multiple saturation pulses with the same phase as the  $90^\circ$  pulse of the CPMG sequence, with the signal of the desired coherence pathways can be generated  $90^\circ$  out of phase with respect to the spurious signal. Hence, the signals can also be separated by phasing the receiver as described for the inversion-recovery sequence.

In the absence of a recycle delay, and neglecting the detection time (duration of the CPMG sequence), the saturation-recovery sequence requires an experimental time of about  $2.5T_1N_{\text{pts}}$  for a linear stepping of  $\tau$ , and just  $T_1N_{\text{pts}}$  for a logarithmic one. In this way, this sequence is six times faster than the inversion-recovery sequence. Considering that the  $T_1$  curve measured with the inversion-recovery sequence has a range of about  $1.5M_0$  (this range may be smaller if  $B_1$  is inhomogeneous) and that the range measured by saturation recovery is  $M_0$ , two scans of the saturation recovery are needed to approximately compensate for the sensitivity difference. At the same sensitivity, the saturation recovery is three times faster than the inversion-recovery variant.

While a single-echo detection requires, in general, a large number of scans that lead to extremely long experimental times, multi-echo detection achieved by applying a train of refocusing pulses after the  $T_1$  editing sequence considerably reduces the measurement time. A critical issue that must be taken into account when a long echo train is added is the possible presence of multiple  $T_1$  times in the sample. If the different  $T_1$ s show similar  $T_2$ s then the echo train addition leads to a  $T_1$  build up curve where the fractions of the  $T_1$ s are preserved. However, if spins with a short  $T_1$  have also a short  $T_2$  and the length of the echo train is set to sample the long  $T_2$ , then the signal amplitudes are weighted to the limit that the short  $T_1$  may even

disappear from the buildup curve. To preserve the amplitude ratio between the two or more  $T_1$  components, the number of echoes to be added must be small enough so that one cannot observe an appreciable signal decay of the shortest  $T_2$  component during the echo train. If the number of echoes is not properly set, it is expected to affect the signal amplitude ratio, but the  $T_1$  values extracted from the curve remain unaffected.

### 2.2.5 Diffusion Measurements

Magnetic field inhomogeneity has been pointed out to be disadvantageous in single-sided NMR because resonance offsets across the sample complicate the performance of conventional pulse sequences [1–4] and reduce the sensitivity during the detection period [23]. However, some applications like high-resolution sample profiling or the measurement of diffusion coefficients benefit from strong field gradients.

A difficulty faced in the early days of single-sided NMR when trying to exploit the static gradient of open magnets for these types of measurements was the generation of uniform gradients. However, this requirement has been successfully achieved with a number of magnet geometries in the last years (see Chap. 4). In this section, we describe how the echo formation in the presence of a strong and uniform static gradient can be exploited to encode self-diffusion, a parameter that can be used to reveal molecular dynamics and sample microstructure. The effect of molecular self-diffusion on the amplitudes of Hahn and stimulated echoes generated in the presence of a static magnetic field gradient has been analyzed theoretically and experimentally since the very early days of NMR, and the working principle is much older than MRI itself [5, 12, 13]. The use of strong static gradients, such as the one found in the stray field of superconducting magnets, allows measurements of root-mean square molecular displacements as small as 20 nm and self-diffusion coefficients as small as  $10^{-16}$  m<sup>2</sup>/s. Large gradients simplify measurements of the diffusion coefficient in heterogeneous materials such as porous materials and biological systems, since it reduces the relative contribution from background gradients due to susceptibility variation across the sample. This is true because the background gradients are proportional to the magnitude of the applied static field  $B_0$ , but essentially independent of the field gradient. From this point of view, measurements with unilateral low-field NMR sensors, which produce relatively strong field gradients, offer an interesting advantage over conventional methods.

The pulse sequences typically used are based on the generation of Hahn (SE) [5, 12] and stimulated echoes (STE) [13], both operating in the presence of a steady gradient (see Fig. 2.16). To improve the sensitivity of these experiments, a CPMG sequence is applied after the main diffusion-editing period to generate an echo train that takes advantage of long transverse relaxation times of liquid samples.

Thanks to the sensitivity improvement achieved by adding the echo train, complete diffusion curves can be measured in times shorter than a minute for protonated



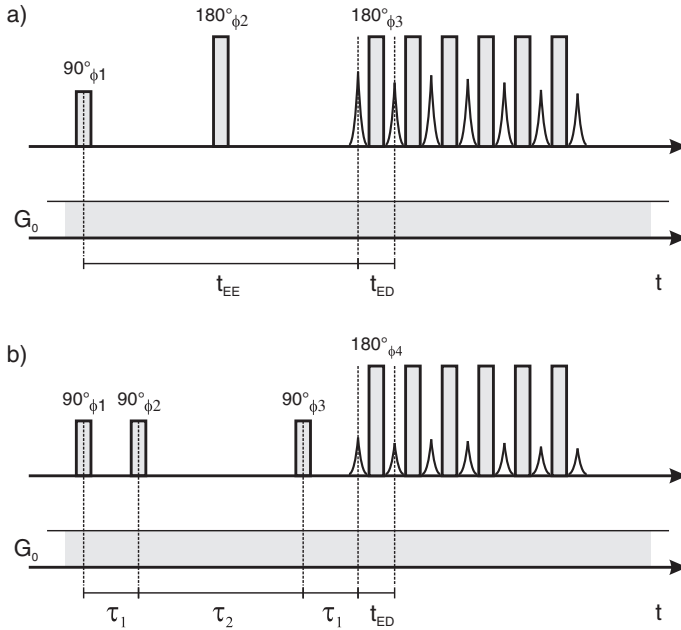


**Fig. 2.16** Diffusion editing pulse sequences based on the generation of a Hahn echo (a) and a stimulated echo (b) in the presence of a static gradient. After the generation of the echo with an amplitude attenuated by diffusion, a train of refocusing pulses is applied to generate a train of echoes that can be added to improve sensitivity. To set the right timings the center of the SE and STE echoes defines the zero time or center of the 90° pulse in a conventional CPMG sequence

solvents. The normalized signal attenuations for the SE and the STE are given by [17, 24]

$$\ln \left( \frac{S}{S_0} \right) = -\frac{1}{12} \gamma^2 G_0^2 t_{EE}^3 D - \frac{t_{EE}}{T_2} \quad (2.21)$$

and

$$\ln \left( \frac{S}{S_0} \right) = -\gamma^2 G_0^2 \tau_1^2 \left( \tau_2 + \frac{2}{3} \tau_1 \right) D - \frac{2\tau_1}{T_2} - \frac{\tau_2}{T_1}. \quad (2.22)$$

The time delays  $t_{EE}$ ,  $\tau_1$ , and  $\tau_2$  are defined in Fig. 2.16. The normalization signal  $S_0$  corresponds to the amplitude of the echoes at very small times  $t_{EE}$  and  $\tau_1$  for SE and STE, respectively. The amplitudes of the Hahn and stimulated echoes are attenuated by the transverse and longitudinal relaxation times (see Eqs. (2.21) and (2.22)). For large values of  $D$ , like in the case of less viscous liquids, and for strong magnetic field gradients, the diffusion terms in Eqs. (2.21) and (2.22) dominate over

the relaxation terms. Furthermore, if  $t_{EE}$ ,  $\tau_1 \ll T_2$ , and  $\tau_2 \ll T_1$ , the echo amplitude in Eqs. (2.21) and (2.22) is governed by the first term on the right side.

Although in absence of relaxation, the spin echo is a factor two larger than the stimulated echo, there are certain cases where it is convenient to implement the STE sequence to measure diffusion. As described by Hahn [5], the amplitude of the stimulated echo relaxes with  $T_1$  during the evolution period  $\tau_2$ , when the magnetization is stored as longitudinal magnetization. Thus, in systems where  $T_1 > T_2$ , it might be advantageous to measure the diffusion attenuation of the stimulated-echo rather than that of the Hahn echo [13]. This is particularly the case in viscous liquids, where a short  $T_2$  is combined with a small diffusion coefficient. For single-sided sensors, the most important advantage of the STE sequence compared to the Hahn echo is that even in the presence of a steady gradient, the STE sequence still consists of two encoding periods separated by a well-defined evolution time when diffusion takes place.

To sample the attenuation caused by diffusion on the Hahn echo amplitude in a steady gradient, the echo time has to be systematically increased in a defined range. By doing so, each point of the diffusion curve is measured for a different diffusion time, allowing the molecules to travel longer and longer distances for increasing echo times. In the stimulated echo sequence,  $\tau_2$  can be set long enough in order to require an encoding time  $\tau_1$  much shorter than  $\tau_2$ . In this way, by increasing  $\tau_1$ , the diffusion curve can be sampled without appreciably varying the total diffusion time ( $\tau_1 + \tau_2$ ), which in this case is defined by  $\tau_2$ .

The possibility to define the diffusion time is extremely useful when studying molecular diffusion in the presence of restrictions or physical barriers like in the case of water or oil diffusing in the porous matrix of rocks. Extensive work done by Mitra and Sen [25, 26] showed that the dependence of the effective diffusion coefficient  $D(L)$  on the molecular mean displacement  $L$  in the time  $\tau_2$  is linear for small  $L$ , and the slope is proportional to the surface-to-volume ratio of the porous material. A measurement of  $D$  vs.  $L$  simply requires measuring diffusion curves as a function of the evolution time ( $\tau_2$ ). In order to sample the diffusion curve properly, the variation range of the encoding time  $\tau_1$  has to be adapted as the evolution time is increased. Since the minimum  $\tau_1$  is positive (actually it is at least the pulse length  $t_p$  plus few microseconds needed by the spectrometer in between rf pulses), the maximum evolution time accessible to the technique is either limited by  $T_1$  or by the dynamic range of  $\tau_1$  (for excessively long  $\tau_2$  the minimum  $\tau_1$  already leads to important signal attenuation). For example, for water measured with a  $G_0 = 20$  T/m and a  $t_p = 5 \mu s$ , the maximum evolution time  $\tau_2$  is about 100 ms. To reach longer evolution times it is convenient to work under a lower  $G_0$ . On the other hand, to reach extremely short evolution times (free diffusion limit), a strong gradient is required. Thus, in most cases a combination of two different sensors may be convenient. To access shorter diffusion times, the direct echo of the CPMG sequence can be exploited [27], in this case the diffusion time is set by the echo time of the sequence.

As we have already discussed in this chapter, the application of a series of rf pulses generates a number of coherence pathways weighted by different relaxation

and diffusion factors. To make sure that the signal measured during the CPMG detection sequence has acquired a defined diffusion attenuation during the diffusion editing period (Hahn or STE sequence) a proper phase-cycle has to be used to select only the pathway generating the Hahn- or the stimulated echo. We have already described how to exploit the particular dependence of each pathway on the phase of the rf pulses in order to select a given signal. However, we have to point out here an important difference to the procedure explained in Sect. 2.2. As we know, after the second pulse of the Hahn echo sequence, there are nine coherence pathways and only two generate a signal. Thus, a simple add/subtract phase cycle suffices to separate them. However, in the present case, as a number of rf pulses is applied after the generation of the Hahn echo, it is not enough to implement a phase cycle that eliminates the pathways generating non-desired signals after the second pulse. We have to make sure that also those pathways that either do not fulfill the echo condition after the second pulse ( $M_{0,+1,+1}$  or  $M_{0,-1,-1}$ ) or are stored as longitudinal magnetization by the second pulse ( $M_{0,\pm 1,0}$ ) are also eliminated. It is so because they can simply generate signals when the CPMG is applied. An example is the pathway  $M_{0,-1,-1}$ , although it does not generate signal after the second rf pulse, a fraction of it is converted into  $M_{0,-1,-1,+1}$  after a third pulse is applied. Hence, the strategy to design a proper editing sequence requires cancelation of every pathway except the one encoding the desired information. Table 2.4 provides the phase cycle required to select the coherence pathway generating the Hahn echo and which eliminates the rest.

The add/subtract phase cycle of the first pulse eliminates the pathways where the magnetization stays as longitudinal magnetization after the first pulse. From the pathways that evolve as transverse magnetization after the first pulse ( $M_{0,\pm 1}$ ), we need to eliminate the ones stored as longitudinal magnetization and the ones that are not affected by the second pulse. This is achieved by exploiting their different dependence on  $\phi_2$ . Cycling the phase of the second pulse from 0 to  $\pi$ , the first group is canceled after the first four phase steps. Then, repeating these four steps but with a  $\phi_2$  incremented by  $\pi/2$ , the magnetization that is not affected by the second pulse is separated from the desired pathway. Although it is true that the unwanted echoes are generated at different times, and may not overlap for a particular  $t_{EE}$  and  $t_{ED}$ , in a diffusion experiment  $t_{EE}$  is varied over a defined range and for certain values

**Table 2.4** Phase cycle to select only the direct echo in a Hahn echo sequence

$\phi_1$	$\phi_2$	$\phi_3$	$\phi_{rec}$
0	$+\pi/2$	$\pi/2$	$\pi$
$\pi$	$+\pi/2$	$\pi/2$	0
0	$-\pi/2$	$\pi/2$	$\pi$
$\pi$	$-\pi/2$	$\pi/2$	0
0	0	$\pi/2$	0
$\pi$	0	$\pi/2$	$\pi$
0	$\pi$	$\pi/2$	0
$\pi$	$\pi$	$\pi/2$	$\pi$

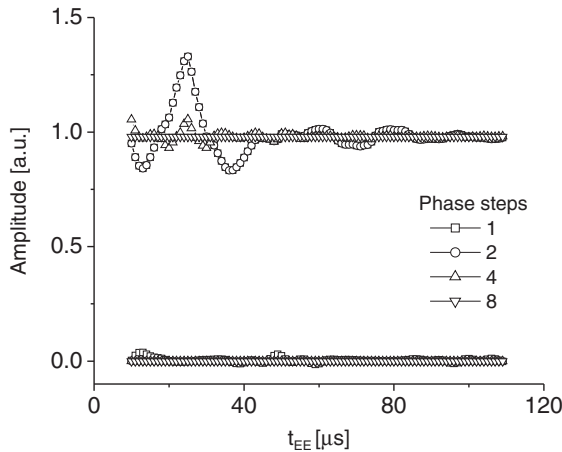


**Fig. 2.17** Signal amplitude obtained by addition of 32 echoes generated by the multi-echo train applied after the Hahn echo sequence of Fig. 2.16 with a  $t_{ED} = 50 \mu s$  plotted as a function of the encoding time  $t_{EE}$  (in absence of diffusion and relaxation). When a single scan is used, the full coherence pathways interfere during the echo train and give rise to variations in the amplitude that depend on  $t_{EE}$ . The first step (two scans) eliminates the signal coming from pathways that stay as longitudinal magnetization after the first rf pulse. In this case, this signal is in the real channel (the desired pathway is along the imaginary channel). Cycling the phase of the second rf pulse in steps of  $\pi$ , the stimulated echo is eliminated. Finally, the coherence pathways converted into transverse magnetization by the first pulse, but untouched by the second one are eliminated by shifting the phase of the second pulse by  $\pi/2$  and repeating the first four steps

the signals can overlap. Moreover, when a CPMG train is used for detection, the unwanted coherence pathways superimpose sooner or later during the train. Then, when the train is added for sensitivity improvement, the distortions are observed as oscillations in the diffusion curve.

The effect of cycling the phases of the different pulses can be observed in Fig. 2.17 where the real and imaginary echo train integrals are plotted as a function of the encoding time  $t_{EE}$  for the different phase steps (with this receiver phase, the desired signal is generated along the imaginary channel, and no signal is expected in the real channel). The largest distortion is introduced by the signal generated by the stimulated echo, but the other two are not negligible and, in general, require elimination.

The same goal needs to be achieved for the stimulated echo sequence. In this case, the pathway generating the stimulated echo must be separated from the remaining 26 pathways. Although in Sect. 2.2 we describe a phase cycle to filter the signals generated after the third pulse, the four steps listed in Table 2.1 do not suffice to ensure that other pathways will not contribute to the signal during the CPMG detection. This is the reason why the 16 steps phase cycle shown in Table 2.5 must be used [19].

**Table 2.5** Phase-cycle to select only the stimulated-echo and eliminate the rest of the pathways after three rf pulses

$\phi_1$	$\phi_2$	$\phi_3$	$\phi_4$	$\phi_{\text{rec}}$
0	0	0	$\pi/2$	$\pi$
$\pi$	0	0	$\pi/2$	0
0	$\pi$	0	$\pi/2$	0
$\pi$	$\pi$	0	$\pi/2$	$\pi$
0	0	$\pi$	$\pi/2$	0
$\pi$	0	$\pi$	$\pi/2$	$\pi$
0	$\pi$	$\pi$	$\pi/2$	$\pi$
$\pi$	$\pi$	$\pi$	$\pi/2$	0
$+\pi/2$	0	0	0	$+\pi/2$
$-\pi/2$	0	0	0	$-\pi/2$
$+\pi/2$	$\pi$	0	0	$-\pi/2$
$-\pi/2$	$\pi$	0	0	$+\pi/2$
$+\pi/2$	0	$\pi$	0	$-\pi/2$
$-\pi/2$	0	$\pi$	0	$+\pi/2$
$+\pi/2$	$\pi$	$\pi$	0	$+\pi/2$
$-\pi/2$	$\pi$	$\pi$	0	$-\pi/2$

### 2.3 The SNR in Inhomogeneous Fields

A common fact to all techniques developed for single-sided NMR is the intrinsic poor sensitivity associated with low and strongly inhomogeneous magnetic fields. From the methodological side it has been shown that the sensitivity can significantly be enhanced by multi-echo detection methods based on the application of CMPG-like pulse trains. By adding the echoes of a train, the measuring times can be reduced by up to two orders of magnitude compared to single echo methods (Hahn echo like) [3, 28]. However, how to optimize the hardware is less obvious mainly because of the lack of a theoretical formulation to quantify the signal-to-noise ratio (SNR) in inhomogeneous fields. Hoult's formulation for the SNR [14] cannot be applied in a straightforward way to single-sided sensors. These sensors are used to study samples much larger than the sensor itself and only a small portion of the sample can be reached in a single experiment. This fact leads to the definition of the sensitive volume, which depends on the magnet, rf-coil geometry, and the pulse sequence applied. The optimization of a magnet requires a delicate balance between field and gradient strength. Clearly a stronger field leads to higher sensitivity, but if it is achieved at expenses of the gradient a smaller sensitive volume is excited, then what happen with the SNR? On the other hand, another typical question that cannot be answered is how much does the SNR improve when replacing a 300 W rf amplifier by 1 kW one?

In this section we present a theoretical formulation for the SNR applicable to single-sided NMR. The size of the sensitive volume is defined considering the rf-pulse excitation bandwidth and the resonance-circuit bandwidth. Furthermore, single- and multi-echo detection sequences are addressed. Finally, an example of how to optimize a single-sided sensor in terms of sensitivity is discussed.

### 2.3.1 The Reciprocity Principle

The SNR of an NMR experiment was initially formulated by Abragam [29], and the analysis was then extended by Hoult and Richards [14]. Although Hoult and Richards give an analytical expression for the SNR, it has been obtained assuming certain aspects that are not valid in the limit of highly inhomogeneous fields. Therefore, a more general expression for the SNR that takes into account off-resonance excitation, inhomogeneous rf fields, and a more general detection scheme has to be derived. In the following, the steps followed in [14] are revised and the assumptions that are not valid for our case are highlighted.

The principle of reciprocity [14] states that a magnetic dipole  $\mathbf{d}$  placed at a point  $\mathbf{r}$  will induce an EMF in a coil given by

$$\xi = -\partial/\partial t\{\mathbf{B}/i \cdot \mathbf{d}\}, \quad (2.23)$$

where  $\mathbf{B}/i$  is the magnetic field per unit of current produced by the coil at the point  $\mathbf{r}$ . In the case of NMR,  $(B_1/i)_{xy}$  is the component of rf field perpendicular to the magnetic field  $\mathbf{B}_0$ , and  $\mathbf{d}$  is the detectable component ( $M_{xy}$ ) of the magnetization per unit of volume  $M_0$  generated after an excitation sequence. If the sample has a volume  $V_s$ , a spatial integration is necessary:

$$\xi = -\int_{V_s} \partial/\partial t\{(B_1/i)_{xy}M_{xy}\}d\mathbf{r}^3 \quad (2.24)$$

In a conventional NMR experiment,  $(B_1/i)_{xy}$  can be assumed to be reasonably homogeneous over the whole sample volume and the excitation is considered to be on resonance; therefore both  $(B_1/i)_{xy}$  and  $M_{xy}$  can be moved outside the integral [14]. Under these assumptions a  $90^\circ$  pulse tips the full equilibrium magnetization, therefore  $M_{xy}$  can be replaced  $M_0$  and the integral is simply the sample volume. However, for the case of a single-sided sensor these conditions are not fulfilled and the integral has to be kept. To solve the integral, the signal response  $\Gamma(B_0, B_1, \Delta f_L)$  for a particular pulse sequence (single pulse, Hahn echo, CPMG, etc.) has to be considered.  $\Delta f_L$  is the rf-circuit bandwidth. The signal response is a complex function that describes phase and magnitude of the transverse magnetization generated by the pulse sequence. The output is measured in units of  $M_0$ , thus  $\Gamma$  is nondimensional and counts the fraction of the equilibrium magnetization that can be detected. The spatial dependence of  $\Gamma$  (sensitive volume) is given by the variations of  $B_0$  and  $B_1$  with position. The effect of the rf-circuit bandwidth is to act as a filter for both excitation and detection and to determine the dead time which imposes a limit on the minimum echo time that can be used in echo sequences.

Equation (2.24) is then written as follows:

$$\xi = -\int_{V_s} \partial/\partial t\{(B_1/i)_{xy}M_0e^{-i\omega_0t}\Gamma(B_0, B_1, \Delta f_L)\}d\mathbf{r}^3. \quad (2.25)$$

In the high-temperature limit the equilibrium magnetization can be approximated by

$$M_0 = N\gamma^2\hbar^2 I(I+1)B_0/3kT, \quad (2.26)$$

where  $N$  is the number of spins per unit of volume,  $\gamma$  is the gyromagnetic ratio, and  $T$  is the temperature of the sample. The RMS noise power generated at the terminals of the rf coil is, in principle, determined only by the thermal noise (Johnson noise). In practice, there are other sources that could induce noise as well. Typical external noise sources are FM radio stations, gradient and shim coils, mechanical devices, NMR spectrometers, and even the sample itself. In the optimum case, the noise induced by external sources can be neglected so that the time-domain RMS noise per unit of frequency,  $\Delta f$ , is purely given by the equation

$$\sigma = \sqrt{4kT\Delta f R}, \quad (2.27)$$

where  $R$  and  $T$  are the resistance and temperature of the coil, respectively. By combining Eqs. (2.25), (2.26) and (2.27) the signal-to-noise ratio can be expressed as

$$\Psi = \left\{ \frac{N\gamma^3\hbar^2 I(I+1)}{6\sqrt{2}(kT)^{\frac{3}{2}}} \right\} \frac{B_0^2}{\sqrt{\Delta f R}} \int_{V_s} (B_1/i)_{xy} \Gamma(B_0, B_1, \Delta f_L) dr^3. \quad (2.28)$$

The expression can be divided into two terms, the first one within the brackets is only determined by the sample properties while the term outside the brackets depends on the hardware and the applied pulse sequence. In the case of homogeneous  $B_0$  and  $B_1$  and a single  $90^\circ$  pulse for excitation, the signal response becomes quite simple.  $\Gamma$  is 1 over the complete volume of the sample and the integral is replaced by  $(B_1/i)_{xy} V_s$ , leading to Hoult's equation [14].

### 2.3.2 Numerical Calculations of the SNR

Based on Eq. (2.28) the SNR can be predicted for different coil and magnet geometries, and in this way a sensor can be optimized in terms of sensitivity. However, from Eq. (2.28) it is quite difficult to visualize the dependence on, for example, the gradient strength, the bandwidth of the resonance circuit, or the rf power. In the following, some common features to single-sided sensors are deduced by means of numerical simulations. First, a relationship between the excited volume and the excitation bandwidth of rf pulses is introduced. The main consequence of this relationship is the decoupling of magnet and rf coil parameters. Second, it is shown that the SNR is maximized when the rf circuit bandwidth matches the excitation bandwidth of the rf pulses. These two main results are used to solve Eq. (2.28) obtaining a more straightforward equation for the SNR.

### 2.3.2.1 Magnet Homogeneity: Excited Volume vs. Excitation Bandwidth

A common observation when working with single-sided sensors is the fact that the higher the rf power output  $W_{\text{rf}}$ , the shorter the rf pulses, and consequently the larger the excited volume, resulting in an increment of the SNR. However, there is a limit ( $W_{\text{rf}} \rightarrow \infty$ ) where the excitation bandwidth is not longer determined by the rf pulse length but by the rf circuit bandwidth (See next section). In spite of that one can still talk in general about the excitation bandwidth,  $\Delta f_{\text{exc}}$ , and its relationship with the excited volume  $V_{\text{exc}}$ . For example, in the case of sensors generating a main gradient  $G_0$  along the depth direction, the relationship is given approximately by

$$V_{\text{exc}} = l^2 \Delta z = \frac{l^2}{\gamma G_0} \Delta f_{\text{exc}}, \quad (2.29)$$

where  $l$  is the lateral size of the rf coil. It is assumed that the rf field does not vary appreciable along the depth direction within the excited slice; typical slice thickness is on the order of few 100  $\mu\text{m}$ . Moreover, the rf field is considered to be constant along the lateral directions over a region of the size of the coil and drops quickly down at the borders of the coil. In general, the lateral selection is an important requirement to this kind of sensors, which are used to obtain depth information [28, 30].

This relationship is quite straightforward to obtain when assuming a 1D problem; however, at first sight, the relation does not have to hold for sensors generating a magnetic field with a sweet spot. In this case, the first-order components of the gradient field (linear terms) are zero and strong quadratic and higher order terms dominate the spatial variations resulting in a complicated “3D” sensitive volume. A quantification of the excited volume considering its shape and dimensions is impractical. Instead, one can compute the magnetic field over a region around the center of the sweet spot and then measure the excited volume simply as the amplitude of a field histogram. In general, the field distribution is centered at the field value corresponding to the middle of the sweet spot. Thus, a simple plot of the maximum value ( $\text{cm}^3$ ) vs. bin size (kHz) shows the relation between excitation bandwidth and excited volume. Figure 2.18a shows the results obtained for a typical magnet geometry generating a sweet spot, the so-called barrel magnet [31]. The same idea, histogram maximum vs. bin size can be used for sensors generating a strong gradient (Fig. 2.18b). While in Fig. 2.18b the proportionality between  $V_{\text{exc}}$  and  $\Delta f_{\text{exc}}$  holds perfectly, in Fig. 2.18a is still a reasonably good approximation.

It is worth mentioning that in both cases  $B_1$  was considered to be homogeneous within the sensitive volume. The assumption of lateral inhomogeneities only modify the proportionality constant ( $l^2$ ) in Eq. (2.29) but not the kind of relationship between the excited volume and the excitation bandwidth, i.e., they remain proportional. Variations along the depth direction are negligible within few 100  $\mu\text{m}$ . In the case of sweet spot magnets, the lateral selection is not an important requirement allowing in general the use of rf coils larger than the size of the sweet spot. Therefore  $B_1$  variations can be considered to be smooth.



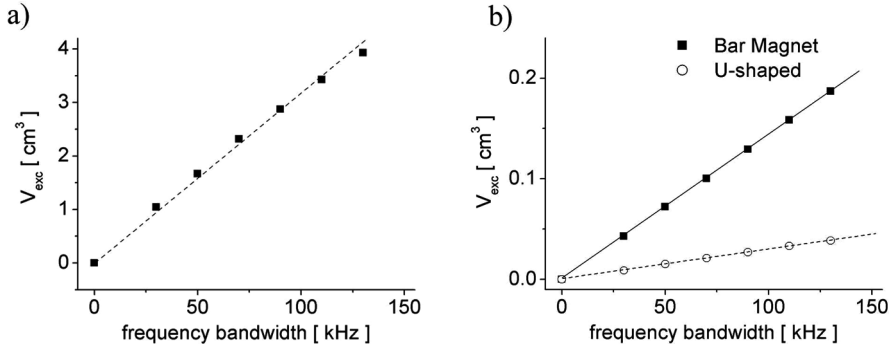


**Fig. 2.18** (a) Excited volume as a function of the frequency bandwidth for the Barrel magnet [31]. The result is obtained by plotting the maximum value of a field histogram vs. the bin size. (b) Same as (a) but for magnets having a strong gradient along the depth direction

For both types of geometries the relation

$$V_{\text{exc}} = V^* \Delta f_{\text{exc}} \quad (2.30)$$

holds, where  $V^*$ , the magnet homogeneity, is the slope of the linear fits in Fig. 2.18. The magnet homogeneity indicates how many cubic centimeters are contained in a frequency range of 100 kHz, or the other way around how large is the frequency spread over a volume of  $1 \text{ cm}^3$ . Equation (2.30) is a fundamental step that allows ones to decouple the magnet parameters from the rf coil parameters. Then, assuming a uniform  $B_1$  over the excited volume, the integral of Eq. (2.28) can be replaced by  $(B_1/i)_{xy} V_{\text{exc}}$  obtaining

$$\Psi = \left\{ \frac{N \gamma^3 \hbar^2 I(I+1)}{6\sqrt{2}(kT)^{\frac{3}{2}}} \right\} B_0^2 V^* \frac{(B_1/i)_{xy} \Delta f_{\text{exc}}(B_1, \Delta f_L)}{\sqrt{\Delta f R}}. \quad (2.31)$$

A direct consequence of it is that one can already compare the sensitivity of different magnets by knowing  $V^*$  and  $B_0$ . In the case of sensors with a strong gradient, the inhomogeneity is only along the depth direction (1D problem) and the SNR can be quantified as  $B_0^2/G_0$ .

### 2.3.2.2 Optimum rf Circuit Bandwidth

The dependence of the SNR on the rf coil parameters is quite complicated in inhomogeneous fields, while in homogeneous fields it is simply  $(B_1/i)_{xy}/\sqrt{R}$ . As already mentioned, the problem is the quantification of the excitation bandwidth, that can be determined either by the length of rf pulses, the circuit bandwidth, or a combination of both. The circuit bandwidth also determines the dead time, which limits the maximum number of echoes that can be acquired in a CPMG train for sensitivity enhancement. Moreover, the coil efficiency  $(B_1/i)_{xy}$  must be considered

not only in the detection but also for excitation; the higher the coil efficiency the shorter the rf pulses. In consideration of the complexity we decided to run numerical simulations to evaluate the SNR. The magnet and rf coil characteristics were taken from the sensor described in [28]. The following assumptions and definitions were used:

- The sequence for detection is a CPMG train of duration  $T_2$ . The excitation bandwidth of the CPMG and Hahn echo sequences are assumed to be the same (see Fig. 2.10), therefore the SNR for the CPMG case is proportional to  $\Psi$  from Eq. (2.31) and the proportionality constant is related to the number of echoes  $n_e$  sampled during the CPMG train. Considering the echoes decay up to one-third of the initial amplitude the SNR can be calculated as

$$\Psi_{\text{CPMG}} = 2/3\sqrt{n_e} \Psi, \quad (2.32)$$

$$\Psi_{\text{CPMG}} = 2/3\sqrt{T_2/(2t_d + t_{\text{acq}})} \Psi, \quad (2.33)$$

where the number of echoes  $n_e$  is the ratio between  $T_2$  and the echo time  $t_E$ . The echo time is chosen to be the shortest one; i.e.,  $t_E = 2t_d + t_{\text{acq}}$ , with  $t_d$  the dead time and  $t_{\text{acq}}$  the acquisition time.

- The dead time is defined as the time needed for the voltage induced in the coil during the application of an rf pulse  $V_{\text{pulse}}$  to reach the RMS voltage generated by the thermal noise  $V_{\text{noise}}$  in the rf coil

$$t_d = (L/2R) \ln(V_{\text{pulse}}/V_{\text{noise}}), \quad (2.34)$$

with  $L$  and  $R$  the coil inductance and resistance, respectively. Although the ratio  $V_{\text{pulse}}/V_{\text{noise}}$  may change from coil to coil and also depends on the applied rf power, its  $\ln$  can be considered to be constant ( $\sim 25$ ). The quantity  $\ln(x)$  changes only 10% per decade near  $x \sim 10^{11}$ .

- The 180° pulse condition

$$\gamma B_1 t_{180} = \pi, \quad (2.35)$$

with

$$B_1 = 1/2(B_1/i)_{xy}\sqrt{W_{\text{rf}}/R}. \quad (2.36)$$

- The rf circuit bandwidth is

$$\Delta f_L = R/\pi L. \quad (2.37)$$

The SNR is calculated taking into account the following steps. The 90° and 180° pulses are calculated using Eqs. (2.35) and (2.36) and choosing the same length for both pulses and half of the amplitude for the 90° pulse. The effects of the

finite circuit bandwidth are considered as a frequency filter acting on  $B_1(\omega)$  for excitation and for detection. Then the echo signal is calculated as the addition of signals coming from different voxels over a volume much larger than the rf coil size. The acquisition time  $t_{\text{acq}}$  is calculated from the echo signal as the time needed to sample the echo from half- to half-amplitude. The acquisition time and the dead time (Eq. 2.34) define the number of echoes  $n_e$ . The frequency bandwidth used to calculate the time domain RMS noise (Eq. 2.27) is calculated as  $1/t_{\text{acq}}$ .

The rf coil resistance is usually modified by including additional resistors in the circuit in order to increase its frequency bandwidth and reduce the Q-factor. In the following the coil resistance  $R$  is used as a variable to control the rf circuit bandwidth. Figure 2.19a shows the dependence of the echo amplitude, i.e., excited volume, as a function of the coil resistance. In the limit  $R \rightarrow 0$  the excited bandwidth is fully determined by the circuit bandwidth, therefore, an incremental change of the resistance is translated one to one (echo amplitude  $\propto R^1$ ) to an increment of the excited volume. In the other limit,  $R \rightarrow \infty$ , the excited bandwidth is determined by length of the rf pulses, which decreases in proportion with  $R^{-1/2}$  (Eq. 2.36). The echo amplitude shows a maximum in the intermedium regime where the rf circuit bandwidth is comparable to the excitation bandwidth of rf pulses. The echo width (Fig. 2.19b) behaves similar to the echo amplitude, in the log-log plot they are horizontally mirrored which reflects the fact that their product is constant. The product is proportional to the spectral spin density, that in this case (strong  $G_0$ ) is the spatial spin density. Figure 2.19c shows the dependence of the echo time of the CPMG train as a function of  $R$ . In the limit  $R \rightarrow 0$  the echo time is determined by both the dead time and the acquisition time. The dead time (Eq. 2.34) as well as the echo width (Fig. 2.19b) is proportional to  $R^{-1}$ , therefore the asymptotic behavior of the echo time is also  $R^{-1}$ . In the opposite limit ( $R \rightarrow \infty$ ) the dead time is negligible and the echo time is dominated by the acquisition time which grows as the  $R^{1/2}$ .

The SNR for the Hahn echo sequence (Fig. 2.19d) does not depend on the coil resistance in the limit ( $R \rightarrow 0$ ) where the circuit bandwidth determines the excitation bandwidth. This fact can be understood by combining the results in the same limit, of Fig. 2.19a and b and considering the detection sensitivity to be proportional to  $(B_1/i)_{xy}/\sqrt{R}$ . The SNR is proportional to the echo amplitude (echo amplitude  $\propto R^1$ ), proportional to the square-root of the acquisition time (acquisition time  $\propto R^{-1}$ ), and proportional to the detection sensitivity ( $\propto R^{-1/2}$ ), hence all different contributions cancel each other. In the opposite limit  $R \rightarrow \infty$ , the contribution due to the echo amplitude is proportional to  $R^{-1/2}$ , the one of the acquisition to  $R^{+1/4}$ , and the detection sensitivity remains unchanged leading to an asymptotic dependence of the SNR proportional to  $R^{-3/4}$ .

Figure 2.19d also shows the behavior for different rf power values. From these results one can conclude that the only influence of increasing the applied rf power is to expand the plateau of maximum SNR toward higher  $R$  values. It is worth mentioning that if the intrinsic coil resistance (no Q-damping) is already in the plateau there is no gain in SNR by increasing the applied power when using a single echo sequence. The situation is different for the case of the CPMG sequence. In this case the echo time determines the maximum number of echoes that can be acquired in the

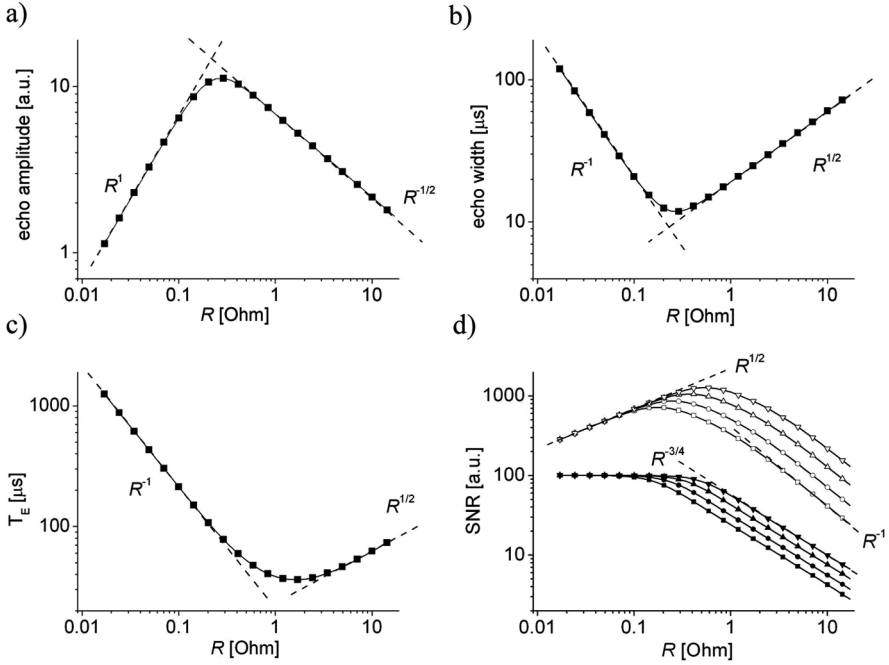


**Fig. 2.19** Dependence of the echo amplitude ( $\propto$  excited volume) (a), echo width (or acquisition time) (b), and minimum echo time of the CPMG sequence (c) on the coil resistance  $R$ . (d) SNR for the Hahn echo sequence and for the CPMG sequence in *solid* and *open symbols*, respectively. From *square* to *triangles* down  $W_{rf}$  is 100, 300, 1,000, and 3,000 W

CPMG (Eq. 2.34). The asymptotic behavior can be simply calculated as the one of the Hahn echo sequence times  $T_E^{-1/2}$  leading to  $\text{SNR} \propto R^{1/2}$  for  $R \rightarrow 0$  and  $\text{SNR} \propto R^{-1}$  for  $R \rightarrow \infty$ . The SNR shows a maximum with a value and a position that depends on the applied rf power. At the maximum there is a compromise between, detection sensitivity, excitation bandwidth, and number of echoes acquired in the CPMG. Interestingly, for the resistance value  $R_{\max}$  that maximize the signal SNR, the circuit bandwidth and excitation bandwidth of the rf pulses are matched, thus

$$\Delta f_L = 1/t_{180} \quad (2.38)$$

which, combined with Eqs. (2.35) and (2.37), results in

$$R_{\max} = \left( \frac{1}{2} \gamma L (B_1/i)_{xy} \right)^{2/3} W_{rf}^{1/3}. \quad (2.39)$$

The condition of Eq. (2.38) for the maximum sensitivity can be introduced in the general expression for the SNR (Eq. 2.28). The ratio between the SNR measured with the Hahn and CPMG sequences is defined in Eq. (2.33), which, considering

$t_{\text{acq}} = t_{180}$ , can be rewritten as

$$\Psi_{\text{CPMG}} = \sqrt{\pi T_2 / k_d} \sqrt{\Delta f_L} \Psi \quad (2.40)$$

with

$$k_d = 9/4 \left( \ln(V_{\text{pulse}} / V_{\text{noise}}) + \pi \right). \quad (2.41)$$

### 2.3.3 An Analytical Solution for the SNR

Based on the issues discussed above, Eq. (2.28) can be combined with Eqs. (2.30), (2.38), and (2.39) to write the SNR as

$$\Psi_{\text{CPMG}} = \left\{ \frac{N \gamma^3 \hbar^2 I(I+1)}{\pi 6 \sqrt{2} (kT)^{3/2}} \sqrt{\frac{\pi T_2}{k_d}} \right\} V^* B_0^2 (B_1/i)_{xy} \left( \frac{\gamma (B_1/i)_{xy}}{2L^2} \right)^{1/3} W_{\text{rf}}^{1/6} \quad (2.42)$$

The term between the brackets  $\{ \}$  depends on the sample properties with the exception of  $k_d$  while the terms outside the bracket depend on the hardware characteristics. The magnet homogeneity  $V^*$  tells one, for example, how many cubic centimeters are contained in a frequency range of 100 kHz. Notice that for sensors with a strong gradient, the inhomogeneity is only along the depth direction (1D problem); therefore, it can be quantified simply as  $1/G_0$ . The term  $B_0^2$  accounts for polarization and induction. The dependence of  $R$  on the frequency (due to the skin depth effect) is not present because the resistance was already optimized to match the circuit and excitation bandwidth (Eq. 2.39). The coil efficiency  $(B_1/i)_{xy}$  appears twice, once to the power of one to account for the detection sensitivity, as in conventional NMR, and once to the power of  $1/3$  to account for the selective excitation. The SNR depends also on the inductance of the coil and the applied rf power, parameters that play no role when working in homogeneous fields.

Equation (2.42) can be used to optimize in terms of sensitivity the magnet and rf coil. The magnet sensitivity  $B_0^2 V^*$  can be obtained in a straightforward way by making a field histogram from a 3D field map around the region of interest as described in Fig. 2.18. The rf coil sensitivity,  $(B_1/i)_{xy}^{4/3} / L^{2/3}$ , is maximized as a function of the coil size and number of turns with the constrain that the coil resistance  $R$  fulfills the condition  $R < R_{\text{max}}$  (Eq. 2.39). The final resistance of the circuit is set to  $R_{\text{max}}$  by adding a resistor to the resonance circuit.

## References

1. Goelman G, Prammer MG (1995, Mar) The CMPG pulse sequence in strong magnetic-field gradients with applications to oil-well logging. *J Magn Reson Ser A* 113(1):11–18
2. Balibanu F, Hailu K, Eymael R, Demco DE, Blümich B (2000, Aug) Nuclear magnetic resonance in inhomogeneous magnetic fields. *J Magn Reson* 145(2):246–258
3. Hürlimann MD, Griffin DD (2000, Mar) Spin dynamics of carr-purcell-meiboom-gill-like sequences in grossly inhomogeneous b-0 and b-1 fields and application to NMR well logging. *J Magn Reson* 143(1):120–135

4. Hürlimann MD (2001, Feb) Diffusion and relaxation effects in general stray field NMR experiments. *J Magn Reson* 148(2):367–378
5. Hahn EL (1950) Spin echoes. *Phys Rev* 80(4):580–594
6. Carr HY, Purcell EM (1954) Effects of diffusion on free precession in nuclear magnetic resonance experiments. *Phys Rev* 94(3):630–638
7. Meiboom S, Gill D (1958) Modified spin-echo method for measuring nuclear relaxation times. *Rev Sci Instrum* 29(8):688–691
8. Ernst RR, Bodenhausen G, Wokaun A (1990) Principles of nuclear magnetic resonance in one and two dimensions. Oxford University Press, New York, NY
9. Kaiser R, Bartholdi E, Ernst RR (1974) Diffusion and field-gradient effects in NMR fourier spectroscopy. *J Chem Phys* 60(8):2966–2979
10. Song YQ (2002, July) Categories of coherence pathways for the CPMG sequence. *J Magn Reson* 157(1):82–91
11. Stejskal EO (1965) Use of spin echoes in a pulsed magnetic-field gradient to study anisotropic restricted diffusion and flow. *J Chem Phys* 43(10P1):3597–3603
12. Stejskal EO, Tanner JE (1965) Spin diffusion measurements – spin echoes in presence of a time-dependent field gradient. *J Chem Phys*, 42(1):288–292
13. Tanner JE (1970) Use of stimulated echo in NMR-diffusion studies. *J Chem Phys* 52(5):2523–2526
14. Hoult DI, Richards RE (1976) Signal-to-noise ratio of nuclear magnetic-resonance experiment. *J Magn Reson* 24(1):71–85
15. Hahn EL (1953) Free nuclear induction. *Phys Today* 6:65–70
16. Hürlimann MD (2001, Apr) Optimization of timing in the carr-purcell-meiboom-gill sequence. *Magn Reson Imaging* 19(3–4):375–378
17. Callaghan PT (1991) Principles of nuclear magnetic resonance microscopy. Clarendon Press, Oxford
18. Coates GR, Xiao L, Prammer MG (1999) NMR logging principles and applications. Halliburton Energy Services. Houston, TX
19. Hürlimann MD, Venkataramanan L (2002, July) Quantitative measurement of two-dimensional distribution functions of diffusion and relaxation in grossly inhomogeneous fields. *J Magn Reson* 157(1):31–42
20. Song YQ, Venkataramanan L, Hürlimann MD, Flaum M, Frulla P, Straley C (2002, Feb) T-1-t-2 correlation spectra obtained using a fast two-dimensional laplace inversion. *J Magn Reson* 154(2):261–268
21. Vold RL, Waugh JS, Klein MP, Phelps DE (1968) Measurement of spin relaxation in complex systems. *J Chem Phys* 48(8):3831–3832
22. Markley JL, Horsley WJ, Klein MP (1971) Spin-lattice relaxation measurements in slowly relaxing complex spectra. *J Chem Phys* 55(7):3604–3605
23. McDonald PJ (1997, Mar) Stray field magnetic resonance imaging. *Prog Nucl Magn Reson Spectrosc* 30:69–99
24. Kimmich R (1997) NMR: tomography, diffusometry, relaxometry. Springer, Berlin
25. Mitra PP, Sen PN, Schwartz LM (1993, Apr) Short-time behavior of the diffusion-coefficient as a geometrical probe of porous-media. *Phys Rev B* 47(14):8565–8574.
26. Mitra PP, Sen PN, Schwartz LM, Ledoussal P (1992, June) Diffusion propagator as a probe of the structure of porous-media. *Phys Rev Lett* 68(24):3555–3558
27. Zielinski LJ, Hürlimann, MD (2005, Jan) Probing short length scales with restricted diffusion in a static gradient using the CPMG sequence. *J Magn Reson* 172(1):161–167
28. Perlo J, Casanova F, Blümich B (2004, Feb) 3D imaging with a single-sided sensor: an open tomograph. *J Magn Reson* 166(2):228–235
29. Abragam A (1983) Principles of nuclear magnetism. Oxford University Press, New York, NY
30. Perlo J, Casanova F, Blümich B (2005, Sep) Profiles with microscopic resolution by single-sided NMR. *J Magn Reson* 176(1):64–70
31. Fukushima E, Jackson JA (2002) Unilateral magnet having a remote uniform field region for nuclear magnetic resonance. US Patent, 6489872

Single-Sided NMR

Casanova, F.; Perlo, J.; Blümich, B. (Eds.)

2011, XIII, 244 p., Hardcover

ISBN: 978-3-642-16306-7